Lauri Nyystilä

Building an EDGE system to the VEBIC laboratories

School of Technology and Innovations
Master’s Thesis
Energy Technology

Vaasa 2024

VAASAN YLIOPISTO
Tekniikan ja innovaatiojohtamisen akateeminen yksikkö
Tekijä: Lauri Nyystilä
Tutkielman nimi: Building an EDGE system to the VEBIC laboratories
Tutkinto: Diplomi-insinööri
Oppiaine: Energiatekniikka
Työn ohjaaja: Anne Mäkiranta
Työn valvoja: Seppo Niemi
Valmistumisvuosi: 2024 **Sivumäärä:** 74

TIIVISTELMÄ:

Ympäristöstä kerättävän datan määrä jatkaa kasvuaan, mikä johtaa pullonkauloihin pilvilaskennassa. Nämä pullonkaulat tulevat erityisesti esiin paikoissa ilman luotettavaa verkkoyhteyttä. Ulapalla matkaava laiva on yksi esimerkki tällaisesta kohteesta. Ongelman ratkaisemiseksi on ehdotettu reunalaskentaa. Tässä opinnäytetyössä käydään läpi kokemuksia reunalaskentajärjestelmän rakentamisesta ja testaamisesta. Lisäksi tutkitaan, voidaanko lämpökameraa käyttää hyödyksi pakokaasuvuotojen havaitsemiseksi laivan konehuoneessa. Opinnäytteessä esitelty työ on tehty konsortiossa oppilaitosten ja yritysten välillä.

Reunalaskennan havainnollistamiseksi rakennettiin järjestelmä, jolla mitattiin värinädataa laivan moottorista. Kaksi kaupallisesti saatavilla olevaa anturipakettia asennettiin kiinni moottoriin. Antureista saatava data lähetettiin langattomasti kahdelle reunalaskentaa suorittavalle laitteelle. Ensimmäinen vastasi datan esikäsittelystä. Toinen suoritti loput vaaditusta laskennasta sekä muutti datan havainnollisempaan muotoon. Pakokaasuvuodoista rakennettiin kaksi erilaista koeasetelmaa. Ensimmäisessä koeasetelmassa keinotekoinen vuoto tehtiin pakokaasuputkeen. Toisessa koeasetelmassa vuoto aiheutettiin moottorin kohdalla ennen turboahdinta.

Reunalaskentajärjestelmä rakennettiin ja testattiin hyvin tuloksin. Testeissä havaitut ongelmat saatiin ratkaistua. Aluksi järjestelmä koostui vain yhdestä reunalaskentaa suorittavasta yksiköstä. Laskentojen kanssa ilmeni kuitenkin ongelmia, minkä seurauksena järjestelmään lisättiin avuksi toinen reunalaskentalaite. Näin reunalaskentajärjestelmä sai lopullisen muotonsa. Ensimmäinen pakokaasuvuotojen havaitsemiseksi rakennettu koeasetelma ei tuottanut tuloksia, joista vuoto olisi ollut havaittavissa. Toisesta koeasetelmasta pakokaasuvuoto voitiin onnistuneesti havaita. Vuoto oli havaittavissa pitkää tarkkailujaksoa käyttämällä.

Työn tulokset huipentuivat siihen, kun toimivaa reunalaskentajärjestelmää havainnollistettiin laboratoriossa. Saatuja kokemuksia käytettiin hyödyksi, kun vastaavanlainen järjestelmä asennettiin matkustaja-alukseen. Tulevaisuudessa erityisesti järjestelmän vakautta pitäisi parantaa. Lämpökameralla voidaan epäsuorasti havaita pakokaasuvuotoja etäältä. Myös vuodon sijaintia putkistossa pystytään arvioimaan. Menetelmän heikkous muodostuu viiveestä, joka oli merkittävä moottorin pienellä kuormalla. Jos vuodon havaitseminen vaatii nopeutta, on hyvä pohtia muita vaihtoehtoja.

AVAINSANAT: reunalaskenta, monitorointi, värähtelyt, pakokaasuvuodot, polttomoottorit, konehuoneet, lämpökamerat

UNIVERSITY OF VAASA			
School of Technology and Innovations			
Author:	Lauri Nyystilä		
Topic of Thesis:	Building an EDGE system to the VEBIC laboratories		
Degree:	Master of Science in Technology		
Major of Subject:	Energy Technology		
Instructor:	Anne Mäkiranta		
Supervisor:	Seppo Niemi		
Graduation Year:	2024	**Pages:**	74

ABSTRACT:

The data gathered from our environment keeps on increasing. The increased data collection creates computational bottlenecks with cloud computing. These bottlenecks are apparent at sites without a stable connection to the internet. One such location is a vessel sailing on the open seas. To solve the issue, an edge computing system is built and demonstrated. Additionally, a thermal camera is tested for exhaust gas leakage detection in the engine room. The work in this thesis was done under a joint consortium of research institutions and companies.

To demonstrate edge computing, a system focused on engine vibration measurements was chosen. Two commercial sensor packages were installed on the engine with a wireless connection to two edge computing units. One edge computing unit was responsible for real time data preprocessing. The other one was used for the rest of the data handling and data visualization. For leakage detection, two different experimental test set-ups were built. The first one focused on exhaust gas leakages in the exhaust gas pipeline. In the second experiment, the leakage was induced before the turbocharger.

The edge computing system was successfully built and tested. Any issues that emerged during system testing were solved. In the beginning, only one edge computing device was installed. At one stage, the fast Fourier transfer calculations stopped working. Another edge device was installed to alleviate the computing tasks, finalizing the development. For leakage detection, the first exhaust gas leakage was not conclusively detectable with a thermal camera. The second experiment resulted in successful detection of exhaust gas leakage. However, the leakage was only detectable over extended periods of time.

The development of an edge system culminated in a working demonstrator built in the laboratory. Later on, the experiences from this demonstration were used in a vessel installation. The future development should focus on improving the overall system stability. With thermal cameras, exhaust gas leakages can be remotely detected. They also allow for leakage position approximation. The weakness comes from the detection lag, which was significant at lower engine loads. If fast leakage detection is required, other exhaust gas detection methods should be considered.

KEY WORDS: edge computing, condition monitoring, vibrations, exhaust gas leakages, internal combustion engines, engine rooms, thermal cameras

Foreword

I thank everyone for their support during the thesis work. Special thanks goes to Seppo Niemi and Anne Mäkiranta for their encouraging support for me to get this thesis done. I am also thankful for all the EDGE project members I got to work with. Especially to Andreas Lundell from Åbo Akademi and Anders Öster from Wärtsilä for the experimental parts of this thesis.

I am grateful for the support from my close colleagues for urging me on with the thesis. I am also grateful for the laboratory team, Sonja Heikkilä and Olav Nilsson, for your assistance and valuable expertise.

To my family and friends: you are irreplaceable for giving me hope and motivation when I had none. Particularly the cheers from Veini that got me through the finish line.

Vaasa, December 2023
Lauri Nyystilä

Table of contents

Figures

Tables

Symbols

f_s	Sampling frequency
n_s	Amount of stored values
N	Rotational speed
p	Pressure

Abbreviations

AWG	Air waste gate
CA	Cam angle
CAC	Charge air cooler
DE	Drive-end
FCV	Flow control valve
FFT	Fast Fourier transfer
FO	Fuel oil
FPA	Focal pane array
HT	High temperature
IR	Infrared
LT	Low temperature
LO	Lubricating oil
MEP	Mean effective pressure
MDAQ	Multi-purpose data acquisition
ML	Machine learning
MSX®	Multi-spectral dynamic imaging
nDE	Non-Drive-end
NN	Neural network
PLC	Programmable logic controller
TC	Turbocharger
VEBIC	Vaasa Energy Business Innovation Centre

1 Introduction

Engine condition monitoring is a vital task performed by experienced crewmembers on a vessel. Over time more and more sensors have been added to the engine room. As a result, it became easier read on what is going on with different parts of the engine system and its auxiliaries. This has led to a situation where vast amounts of data are being stored from different sources, also known as Big Data. The availability of Big Data grants an opportunity to develop data driven predictive maintenance models (Jimenez et al., 2020).

In addition to Big Data, potential predictive maintenance models require two essential components: software to execute the analytics and physical hardware to enable the whole system. Using cloud computing as the sole platform enabler is not feasible for the ship's engine room. Cloud computing requires constant connection to the internet which is not always readily available while traveling far from shorelines. Even when internet connection is established, bandwidth requirements and high latency times cause bottlenecks for these types of systems.

The solution is to add an edge computing system in addition to the cloud. Edge computing enables fast data analytics on site close to the sensors. While heavy lifting is done by edge analytics, the requirements for cloud computing connections diminish. Bandwidth and latency concerns are now greatly reduced. Vital data and pre-processed information are easier to pass on to the shore where its status is closely monitored. New technological methods enable the path towards autonomous engine room.

The purpose of this thesis was to demonstrate how edge computing can be implemented in the engine room. The research was conducted in the Vaasa Energy Business Innovation Centre (VEBIC), a research platform in the University of Vaasa. A research project named *EDGE – Edge Analytics for Smart Diagnostics in Digital Machinery Concept* was established to tackle performance, reliability and efficiency issues with new technologies enabled by edge computing (Krogerus et al., 2018).

2 System description

This section introduces a complete description of existing, utilizable infrastructure as well as new research equipment and systems. The research was enabled by the VEBIC platform, which hosts researchers from multidisciplinary areas. The research platform works on challenges related to energy business, future fuels, energy storage and energy generation. Among else, the VEBIC facilities contain an engine laboratory with one full-sized marine engine, the Wärtsilä 4L20CR.

For research and operational purposes, the engine requires different control and measurement systems. These are operated in the control room of the engine laboratory. The connections and their type are given in Figure 1. A majority of the existing system uses the Modbus TCP/IP protocol, a very common automation control protocol, for signals and commands. For new connections, ethernet connectors and wireless solutions were applied.

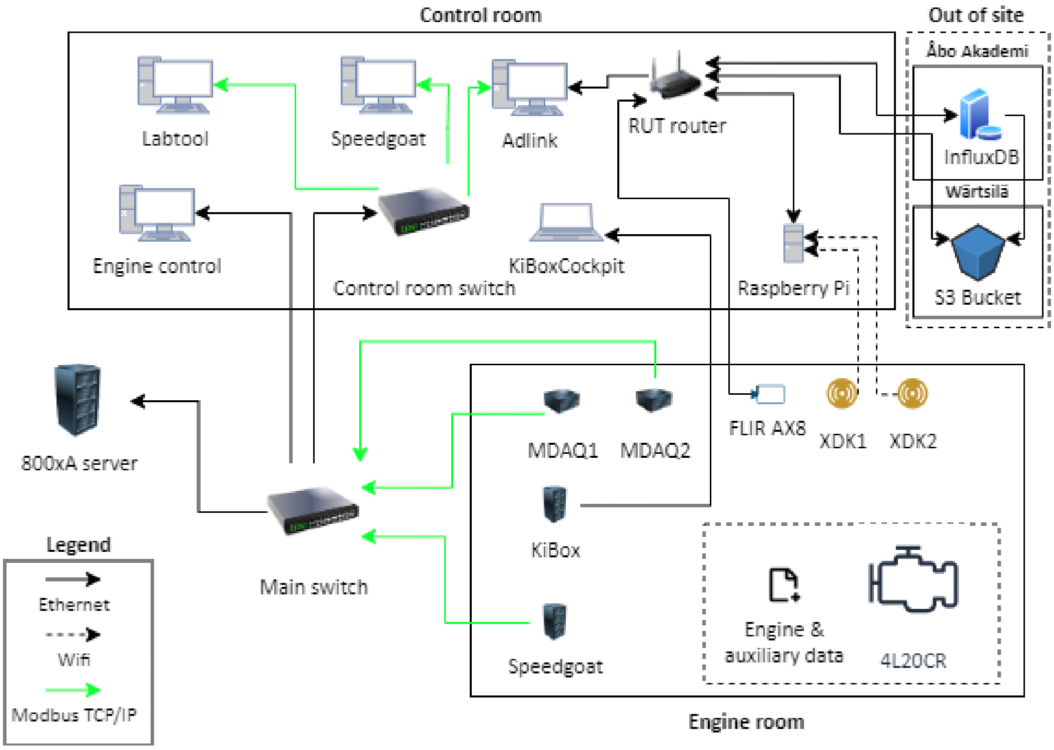

Figure 1. Signal dependencies in the laboratory (legacy parts adapted from Protacon 2019).

2.1 The research engine

The Wärtsilä 4L20CR is a medium speed in-line internal combustion engine with four pistons and a 4-stroke cycle. Compared to a regular Wärtsilä 4L20 engine, it has been modified to include a common rail injection system. The engine is a generating set system, meaning it has an electrical generator and motor combination. It acts as the load generator for the system. Table 1 presents the technical details related to engine output and performance. The rotational speed determines maximum sustainable electrical power output. With 900 rpm the cap stands at 740 kW and with 1 000 rpm at 800 kW. The charged air system contains an intercooler. (Wärtsilä, 2018a).

Table 1. Specifications of the Wärtsilä 4L20CR engine (adapted from Wärtsilä, 2018a).

Property	**Value**
Bore	200 mm
Stroke	280 mm
Number of cylinders	4
Number of valves per cylinder	2 for inlet and 2 for exhaust
Piston displacement	8,8 l/cylinder
Engine rotational speed	900 & 1 000 rpm
Sustainable power output	740 kW & 800 kW
Supercharging	Turbocharger (TC)
Engine type	Compression ignited

The engine requires different auxiliary systems around it to ensure reliable operation. Data from these auxiliary systems is widely available and accessible in the control room. In addition, new sensors have been added to capture the vibrations caused by engine operation and a thermal camera to detect possible exhaust gas leakages. An image of the 4L20CR engine in the VEBIC laboratories can be seen in Figure 2.

Figure 2. The Wärtsilä 4L20CR research engine.

2.2 Fast cylinder data

For detailed cylinder pressure curves, the laboratory is equipped with a KiBox To Go by Kistler. According to Kistler (2019, p. 78), it has a sampling speed of 312.5 kHz. However, the sampling series is not saved or viewed as a time-based measurement. Instead, degrees of crank angle (°CA) are used as the unit of measurement. During the full 4-stroke cycle a total of 37 500 pressure measurements are taken. Due to a constrain in the resolution, the values can only be read at 0.1 °CA difference from each other. By using (1) with the engine rotational speed N at 1 000 rpm and 7 200 stored pressure values n_s during the cycle, the system seemingly measures at 60 kHz. This limits the post processing resolution to the value of f_s, since the system keeps re-writing the value at 0,1 °CA until the next point in resolution is achieved.

$$f_s = n_s N \tag{1}$$

As the KiBoxCockPit is set in the control room, it shows the measurement points and calculated values from a range of -60 to 60 °CA. During engine operation, the cylinder pressure curve can be monitored in real time. Any small differences between the shapes of curves or pressure differences are observable. For post processing, the 120° examination range leaves 2 400 measurement points for one cycle per cylinder due to re-writing described above.

2.3 Speedgoat

While traditional Wärtsilä 4L20 engines have a UNIC automation system (Wärtsilä, 2018a), the engine in VEBIC laboratories uses Speedgoat control system for engine control and safety assurance. The system allows tight integration using Matlab Simulink for simulation and experimental confirmation. All engine parameters are operated and supervised through the Speedgoat user interface in the control room, shown in Figure 1.

The Speedgoat system functions as a Modbus slave and master (Wärtsilä, 2016), depending on the task at hand. This configuration lets the Speedgoat system to control multipurpose data acquisition (MDAQ) data collection modules while at the same time working as Modbus slave for the programmable logic controller (PLC) and Labtool.

2.4 The PLC

The PLC is responsible for controlling all the auxiliary engine systems in the engine room, such as engine pre-heating, cooling system and the fuel system. Additionally, the PLC handles laboratory’s ventilation and its chimney’s purging. The PLC’s main component is the ABB AC 800M controller unit. A simplified connection scheme to the PLC is presented in Figure 1.

Like the Speedgoat system, the PLC is built from several different modules. Each module has its specific purpose and can be replaced or upgraded if needed. Examples of module units are the controller module, communications module and I/O module. Together, the PLC and Speedgoat systems are responsible for every aspect of the Wärtsilä 4L20CR engine control.

2.5 Edge devices

For edge calculation purposes, two different computing units were installed. A light Raspberry Pi and a more rugged industrial computing unit, Adlink MXE-5400 series. These units are close together, and connected via the RUT router presented in Figure 1.

2.5.1 Raspberry Pi

A Raspberry Pi 4 Model B handles data pre-processing before transferring it forward. The pre-processing was initially intended all to be done by the Adlink device, but due to errors with fast Fourier transfers (FFT), part of the calculations is shifted. Hence, an additional processing unit was installed. The Raspberry Pi is connected to the two XDK110's with a Wi-Fi connection. Technical details of the device are presented in Table 2.

Table 2. Technical specifications of the Raspberry Pi 4 Model B (adapted from Raspberry Pi Ltd, 2019).

Features & interfaces	**Details**
Central processing unit	ARM quad core A72 clocked at 1,5 GHz
Memory	Gigabyte LPDDR4R SDRAM
Storage	SD card slot
Ethernet port	Gigabit, support for power over ethernet
Wireless LAN	802.11 b/g/n/ac
Graphical processing unit	VideoCore VI 3D Graphics
Dual HDMI display output	Up to 4K60p
USB ports	2 x USB2, 2 x USB3
GPIO	28 pins supporting a range of interface options

The Raspberry Pi was installed in the control room for several reasons. Primarily, its exposed circuit board would require a protective casing if installed close to the engine, where likelihood of oil or other spills is non-negligible. Secondly, the Wi-Fi connection in both XDK sensors and the Raspberry Pi (Figure 3Figure 3) allowed for easier installation with less cable management. Lastly, in a case where the device stops working, troubleshooting directly from the control room is far more convenient compared to other options.

Figure 3. Raspberry Pi 4 Model B in the control room.

2.5.2 Adlink

The main bulk of the edge processing is implemented in the Adlink MXE-5401/M16G embedded industrial computer. It's external heat dissipators allows the system to be completely fanless, being optimal for harsher than normal conditions. The system endures engine room conditions, being able to operate with an ambient temperature of 50 °C (Adlink Technology, 2013). More detailed specifications are listed in Table 3.

Table 3. Technical specifications of the Adlink MXE-5401/M16G (adapted from Adlink Technology, 2013).

Features & interfaces	Details
Central processing unit	Intel Core i7-4700EQ
Chipset	Intel Mobile Platform Controller Hub (QM87)
Memory	4 GB DDR3L 1600 MHz SODIMM module
Storage	2 x SATA-III 2,5” HDD/SSD slots, 1 x CFAST slot, 1 x eSATA interface connector
Ethernet port	4 X GbE ports
Serial ports	2 x RS-232/422/485 COM ports, 2 x RS-232 COM ports.
Display output	2 x Dual Mode DisplayPort, 1 x VGA+ DVI with DVI-I connector
Mini PCIe	2 x internal PCIe mini card sockets
USB ports	6 x USB3 outside, 1 x USB2 internal
DI/O	8 x DI/O

The Adlink is connected to the control room network through Modbus TCP/IP (Figure 1). It is also connected to Raspberry Pi and other devices outside the control room through the RUT router. The installed operating system is CentOS 7, a light weight Linux distribution. For data handling, InfluxDB is installed. More details of these two systems are written in Sections 2.9.1 and 2.9.2, respectively.

2.6 XDK110 sensors

The Bosch XDK110 is a compact development kit equipped with various sensors. With built-in lithium ion battery and Wi-Fi connection, it can be installed almost anywhere without wiring for quick testing sessions. Unfortunately, the built-in battery causes some slight limitations. During longer measurement periods, charging of the device is required. This lowers the maximum operating temperature from 60 °C down to 45 °C (Table 4). Hence, positioning limitations exist when installing it on the engine. To mitigate risk if the device breaks down and to validate the vibration data, two XDK110's were installed.

Table 4. Technical specifications of the Bosch XDK110 (adapted from Bosch, 2016).

Features	**Details**
Chipset	ARM Cortex M3
Memory	128 kB
Storage	1 MB Flash, micro SD-slot
Battery	Lithium ion 560 mAh
Wireless LAN	IEEE 802.11b/g/n
Bluetooth	4.0 IEEE 802.15.1
Operating conditions	
Temperature range	-20 – +60 °C
Temperature range while charging	0 – 45 °C
IP rating	IP 30 (IEC 60529)

As the XDK110's purpose is to measure engine vibration levels, the accelerometer is the most critical of all the sensors included. It has a maximum sampling rate of 2 kHz with a measurement range of ±2 – ±16 g (Bosch, 2016). However, the maximum sampling rate for programmable signals is 500 Hz (A. Lundell, personal communication, November 17, 2020). Table 5 lists all Bosch XDK110's included sensors and their producers.

Table 5. The sensor list of Bosch XDK110 (Bosch, 2016).

Instrument	**Producer**	**Model**
Accelerometer	Bosch	BMA280
Acoustic noise sensor	Akustica	AKU340

Instrument	Producer	Model
Digital light sensor	Maxim Integrated Products	MAX44009
Environment	Bosch	BME280
Gyroscope	Bosch	BMG160
Inertial sensor	Bosch	BMI160

Due to the fear of leaking oil harming the XDK110 sensors, they were installed next to the generator part of the genset rather than the engine block. At first, the XDK110 closer to the engine (XDK2) was installed below the engine mounts (Figure 4, left). However, soon its permanent position was realized in the same line with XDK1 (Figure 4, right). At the same time, both XDK110's were rotated to face the power port towards control room. They were attached to the genset with a two-sided tape.

Figure 4. The Bosch XDK110's at their original orientation and position (left) and at their final installation (right).

2.7 Router

To handle all the new data traffic between edge devices, a new router Teltonika Networks RUT950 was installed to the control room. It creates a LAN network between Adlink, FLIR and Raspberry Pi. In addition to edge data handling within the laboratory, it allows a connection to the virtual InfluxDB server (Figure 1). Table 6 shows the main features of the RUT950.

Table 6. Technical details of Teltonika Networks RUT950 (Teltonika Networks, 2022).

Features & interfaces	**Details**
Central processing unit	Atheros Wasp, MIPS 74Kc, 550 MHz
Memory	128 MB DDR2
Storage	16 MB
Ethernet	4 x IEEE 802.3, 802.3u ports
Wireless LAN	802.11b/g/n
SIM	2 x SIM slots
Mobile module	4G capabilities, up to 150 Mbps
OpenVPN	Supports multiple simultaneous clients, 12 encryption methods

2.8 Thermal camera

The thermal camera used is a FLIR AX8. It is a commercial level device, capable of producing regular video, thermal video and their combination multi-spectral dynamic imaging (MSX®). As of its capabilities, it has a heat sensing capability from -10 to +150 °C (Table 7) and uses a focal panel array (FPA) with uncooled microbolometer technology. With an electromagnetic detection range from wavelengths between 7.5 to 13 µm, it catches a wide range of infrared (IR) radiation. All technical details of the FLIR AX8 can be found in Appendix 1.

Table 7. FLIR AX8 technical specifications (modified from Teledyne FLIR, n.d.).

Attribute	**Details**
Object temperature range	-10 to +150 °C
IR resolution	80 x 60
Image streaming resolution	640 x 480
Spectral range	7.5 – 13 µm
Detector type	FPA, uncooled microbolometer
Image storage mode	IR, visual, MSX®

The purpose of the use of FLIR AX8 was to investigate if commercial thermal cameras can be used for exhaust leakage detection; additionally, if it can be used to detect leaking liquids, whether it’s lube oil (LO), fuel oil (FO) or cooling water. For the exhaust gas leak, the wish was to see the area around the leakage to heat up to greater temperatures compared to the surrounding area. For a regular maritime engine, the surface area should not exceed 60 °C (A. Öster, personal communication, November 8, 2019), allowing the thermal camera to operate well within the detection range. However, the VEBIC laboratory engine is not completely thermally shielded, and surface temperatures can exceed 100 °C.

The thermal camera was connected to the Adlink through the RUT router (Figure 1). It was completely controlled through a web-interface and saved the recorded files to Adlink. It was attached to a rail and used for two different exhaust gas leak detection set ups.

2.9 Software

The Adlink computer was installed with a CentOS 7 operating system and InfluxDB for edge data management. As for the VEBIC control room’s data logging and measurement development, Labtool was used.

2.9.1 CentOS

Noviantika (2023) notes CentOS as a Linux distribution that is modified from the Red Hat Enterprise Linux (RHEL). It is open source, reliable and boasts a high security level. An active community supports the development of CentOS. Only small changes from RHEL are made, as the focus is on keeping full compatibility between the two systems (CentOS, n.d.). As such, the CentOS is a robust choice for experimental edge computing purposes.

2.9.2 InfluxDB

According to Aasen (2017), InfluxDB is a time series database capable of handling hundreds of thousands of new data points per second and storing them efficiently. It is part of the TICK Stack product family, published by InfluxData. In addition to InfluxDB, the TICK Stack consists of Telegraf, Chronograf and Kapacitor. Each part of the TICK Stack can be utilized separately, but together they form a comprehensive data management system.

On Telegraf, Aasen (2017) notes it being a data collection unit, supporting data gathering from different sources. InfluxData (n.d.-b) divides Telegraf’s operation in four different steps. First, it receives the data from any of the chosen input sources. Next it is transformed and filtered. Thirdly the data is congregated with minimum, maximum and mean values taken. Lastly the data is sent forward in desired format.

In VEBIC, the data from Telegraf was sent to Kapacitor, where alerts data could be validated and processed (A. Lundell, personal communication, January 14, 2021). Kapacitor can also be used for creating alerts and applying machine learning (ML) algorithms (InfluxData, n.d.-a). After proper processing, data from Kapacitor was directed to local InfluxDB and Chronograf and a cloud based Telegraf, where it could remotely be processed.

Lastly, Aasen (2017) notes that Chronograf is an user interface for the whole TICK Stack ecosystem. Data can be visually observed through modifiable dashboards and alarms for Kapacitor created. A. Lundell (personal communication, April 18, 2019) adds that Chronograf works as an administration console in TICK Stack.

2.9.3 Labtool

Labtool is a robust data collection and trend following software. It graphically visualizes how temperatures, pressures and other signals from the engine have evolved over time. It is also used to log values, that require special attention. The logging frequency varies, and is dependent on the source. Both the PLC and Speedgoat write values to Labtool, as it is configured to the system as a Modbus slave.

During the EDGE project, Labtool was mainly used as conventional engine data logging tool. However, since communication between Labtool and Adlink could not be established (**Virhe. Viitteen lähdettä ei löytynyt.**), the data log files were transferred after engine runs manually using USB-sticks. The gathered data was then post-processed and evaluated.

2.10 Signals

During the project, the method evolved for how certain thresholds would be measured constantly. One aspect was to try to reduce the ways in which the on-board crew would be required to do regular check-ups (Wärtsilä, 2018b). Installation of new sensors was initially suggested for all measurement subjects. However, in most cases it was sufficient to use a combination of existing sensors. The only requirement was establishing access to the Modbus network between the sensors and the PLC or Speedgoat.

To establish which signals are the most important for engine condition monitoring, experts from Wärtsilä were consulted. With the assistance provided, the original signal list shrank from over 800 possible signals down to the 164 most important.

This section discusses some of the signals and measurement points, that should be established to the Adlink device for edge computing. The complete list of signals can be found in Appendix 2.

2.10.1 Water expansion tank

One issue is following the water level in the water expansion tank. Traditionally, the level is checked visually through a reader attached to the expansion tank. Furthermore, there are sensors detecting if water level reaches a minimum or maximum level in the tank. There is no method of knowing what the exact level is without visually inspecting the reading next to the tank. Therefore, it was suggested to add a static pressure sensor to the bottom of the water expansion tank to detect sudden, unexpected changes in the water level. Eventually the solution for this issue is to follow the rate of alarms created by the system. The responsibility of edge computing is to know whether the rate of alarms is at regular levels, or if abnormal behaviour is present.

2.10.2 Lubricating oil level in the sump

In the VEBIC 4L20CR engine, an oil dipstick measures the lubricating oil (LO) level in the sump. This task should be done every 50 engine running hours (Wärtsilä, 2018b). A static pressure sensor was acquired to replace the manual measurements. However, a special mount is required to attach the pressure sensor safely in the engine. There were not any pre-designs for this engine type and new drawings would be required to achieve the right mount size and position inside the engine. Unfortunately, no proper designs for the mount were successfully obtained during this project.

2.10.3 Leaked fuel oil quantity

During the regular engine operation, fuel is constantly circulating from the day tank to the engine and back to the day tank. Additionally, small amounts of fuel leak from the injection pumps and valves and is drained from the engine (Wärtsilä, 2018a). Depending on the type of fuel, the installation may require different instruments in the leaked fuel line. Mainly diesel-type low viscosity fuels are used in the 4L20CR, but occasionally higher viscosity fuels can be used. Due to this, a fuel cooler is needed in the return fuel line. It prevents the viscosity of the fuel from dropping too low for operation (Wärtsilä, 2018a).

The leaked fuel oil quantity is an important metric when determining the overall status of the engine. During regular engine operation, the clean leak fuel amount is stated as 2.16 kg/h according to Wärtsilä (2018a). The fuel drains into a clean fuel leak. The experience with VEBIC 4L20CR showed a drastically lower clean fuel leakage than expected. Any sudden change in the amount of clean fuel leak is therefore essential. The clean leak fuel tank has upper and lower limit sensors, the alarms of which are identified in the automation system and will be used to detect anomalies in the leaked clean fuel amounts.

In rare cases while operating a regular 4L20CR engine, fuel may spill in the hot box of the engine (Wärtsilä, 2018a). This will cause dirty fuel leakage, which must be treated separately from the clean fuel. While following the amount of these type of leakages would be in line with the project’s work, the low running hours of the engine and relatively low amount of leakages resulted in focusing only on the clean fuel leakages.

2.10.4 Fuel pressure drop over filters

There are two different fuel filters in the FO line. One is an automatic filter and the second one is a fine filter. Both filters require maintenance from time to time. To indicate when time for clean-up starts to be near, pressure sensors are installed before (p_1) and after (p_2) the filter. When the pressure difference

$$p_1 - p_2 = \Delta p \tag{2}$$

is equal to 0.2 bar, it is recommended to clean the filter. At Δ*p* = 0.8 bar an alarm is triggered by the automation system. If no alarm system is installed, it is recommended to check the Δ*p* value every 50 operating hours (Wärtsilä, 2018b).

It was suggested to follow the rate of alarms in the long run to establish a baseline for edge computing. Unfortunately, the FO filter pressure signals do not exist in the Modbus network, but are separate from it. Therefore, they were not added in the full list of signals (Appendix 2).

2.10.5 Lubricating oil pressure drop over filters

The engine's circulating LO is treated in an automatic LO filter and a centrifugal filter. According to Wärtsilä (2018b), the Δ*p* over LO filters needs to be checked every 50 hours and the filters cleaned if necessary. Additionally, the filter candles are supposed to be cleaned every 4000 engine running hours and the worn parts changed.

As there is a pressure sensor before and after automatic LO filter, a similar approach as with FO filter can be made. The Equation (2) applies and rate of alarms can be followed. A baseline for alarm rates will need to be established with longer timeframes. Any rate change in alarms indicates a status change and requires investigation.

2.10.6 Checking the function of automatic pre-lubrication

In a regular 4L20CR engine, the function of automatic pre-lubrication needs to be checked daily by running it (Wärtsilä, 2018b). Because the signal for automatic pre-lubrication could be located through the Modbus network, it was suggested to create a small program that keeps track on the signal. If the pump has not been turned on by a certain time threshold, it could either be programmed to run the pump by itself or inform the operators to check it.

3 Experiments and testing

Separate engine runs were conducted to validate the edge computing system. Besides the purposeful edge computing runs, the research engine was used for other experiments. Depending on the experiment or engine run in question, the data was gathered as well if possible. This section presents the schedule for engine runs, how the vibration data was gathered, experimental set-up for thermal imagery and the existing signal network. It was of a high importance to gain data on the basic operation; for instance, how the temperatures develop as the engine heats up and how does the vibration data look at different load points.

3.1 Engine runs

The engine was running for various reasons during the data gathering periods. The exact reason for running the engine could not always be disclosed. Similarly, the data for all engine runs could not either partially or completely be studied due to confidential reasons. Table 8 shows the dates on which the engine was running. Included are the start, stop and reason for running the engine, when applicable. In the end, a total of 51 engine runs were conducted.

3.2 Vibration data

The vibration sensors were used to get the normal engine running scenarios. Therefore, they were running constantly to catch any scenario the engine could be running, in addition to engine runs done by the project team members. In cases where there were issues connecting to an XDK110, they were rebooted as soon as possible. Otherwise they were allowed to idle while waiting for the next engine run.

Table 8. The engine run schedule.

Date	Start	Stop	Reasons for running the engine
11.6.2019			
12.6.2019			
19.6.2019			
20.6.2019			
24.6.2019			
4.11.2019			
5.11.2019			
6.11.2019			
7.11.2019			
8.11.2019			
11.11.2019			
12.11.2019			
13.11.2019			
27.11.2019	10:53:00	12:11:00	FLIR, no leak
28.11.2019	12:32:00	14:07:00	FLIR, leak
9.12.2019	12:55:00	14:32:00	
12.12.2019	08:46:00	12:27:00	
17.12.2019	13:31:00	15:22:00	Flushing the cooling system
18.12.2019	10:56:00	13:09:00	Flushing the cooling system
19.12.2019	13:30:00	17:25:00	Flushing the cooling system
9.1.2020	13:20:00	15:17:00	Flushing the cooling system
13.1.2020	13:27:00	16:18:00	Flushing the cooling system
6.2.2020	10:15:00	10:47:00	Flushing the cooling system
13.2.2020	09:48:00	11:44:00	Flushing the cooling system
20.2.2020	13:15:00	15:08:00	FLIR test, injector failure
21.2.2020	13:19:00	14:07:00	Start-up test
3.3.2020	12:23:00	13:39:00	FLIR, no leak
4.3.2020	10:05:00	11:25:00	FLIR, leak
12.3.2020	12:17:00	13:40:00	FLIR, leak
16.3.2020	09:46:00	11:02:00	FLIR, no leak
16.3.2020	11:02:00	12:48:00	Speedgoat testing
17.3.2020	15:51:00	16:12:00	System testing
9.4.2020	09:53:00	12:32:00	Injector testing
15.4.2020	12:11:00	15:03:00	Injector testing
29.4.2020	12:06:00	14:08:00	Testing
20.5.2020	12:48:00	15:54:00	Testing
26.5.2020	10:11:00	15:44:00	Running engine
24.6.2020	09:24:00	11:19:00	Testing after injector change
30.6.2020	14:44:00	15:43:00	Exhaust gas temp control
7.7.2020	09:57:00	13:56:00	Exhaust gas temp control
22.9.2020	09:54:00	10:48:00	
22.9.2020	11:16:00	11:42:00	
22.9.2020	13:54:00	15:07:00	
17.11.2020	12:35:00	16:55:00	System testing
19.11.2020	13:56:00	14:53:00	
14.12.2020	09:25:00	10:22:00	Testing, failure
14.12.2020	11:01:00	11:10:00	Testing, failure
15.12.2020	12:48:00	13:07:00	Testing, failure
21.12.2020	15:26:00	15:34:00	Testing, failure
15.3.2021	12:35:00	15:05:00	System testing
16.3.2021	09:28:00	10:43:00	System testing

The goal was to measure the peak vibration frequencies and their amplitudes constantly present while running the engine. Due to the rather small maximum programmable sampling rate of 500 Hz, the focus had to be kept on slower frequencies. This left out all the fast-rotating bearings and other small amplitude, higher frequency rotating parts. This was in-line with the target for having a general engine condition monitoring system.

The raw, measured vibration data is first sent via Wi-fi from the XDK110's to the Raspberry Pi for FFT. Subsequently the vibration data is sent to the InfluxDB, where it is further processed. From InfluxDB the vibration data can be monitored in various ways in the Chronograph. The data is both stored locally on the Adlink and sent out-of-site, allowing real time remote monitoring. After engine running sessions, the data is transferred for long-term storage to the AWS S3 Bucket.

3.3 Thermal imagery

Two different test set-ups were used for thermal imagery experiments. In the first one, a small artificial exhaust gas leakage was produced in the exhaust gas pipeline, at the sample measuring points. For the second thermal imagery experiment, the artificial leakage was produced at the engine, before the TC. In both cases, the engine was operated on two separate days. This ensured uniform temperature when starting the engine. Moreover, a controlled video sample without any artificial leakage was produced as a reference. For consistency, the thermal scale was kept from 20 to 100 °C throughout the experiments.

Due to the high amount of details required for the thermal video and the rather small resolution of 80 x 60 pixels, the chosen image mode was visual MSX®. It highlights details from the higher resolution visual image and adds the thermal feed on top of it (Teledyne FLIR, 2019). The arrangement allows for a higher level of detail than what would otherwise be possible with pure thermal image mode.

The validation of exhaust gas leakage experiments' successes were conducted on the produced infrared video material by human observation. Additionally, ML tools were deployed by another project partner to see if datasets can be used to produce a reliable positive validation case. The used tools are not discussed in depth, but the results on ML validation experiments will be discussed on general level in Sections 4 and 5.

3.3.1 Exhaust gas pipeline

For producing video samples, the thermal camera was mounted on a rail with a clear view to the exhaust pipe's sample measuring points. In Figure 5, a regular image is taken from the position of the thermal camera. The measuring point in question is first from the right. Another rail, closer to the artificial leakage point is also visible from Figure 5. It was first considered as superior over the final filming location. Unfortunately, the rail in question vibrates slightly while the engine is running, causing unstable video quality. Additionally, the final filming location has a better view on the edges of the sample measuring spots, which is essential for the success of the experiment.

To produce an artificial exhaust gas leakage, a capped nut from the measuring point of the exhaust gas sample spot is removed, opening up a free path for the exhaust gas due to slight overpressure in the pipeline (Figure 6). The hypothesis was that as the exhaust gas escapes, it will evidently contact the surrounding edge, heating it up faster compared to the other measuring points. This heat can then be picked up by the thermal camera's FPA sensor, validating the hypothesis.

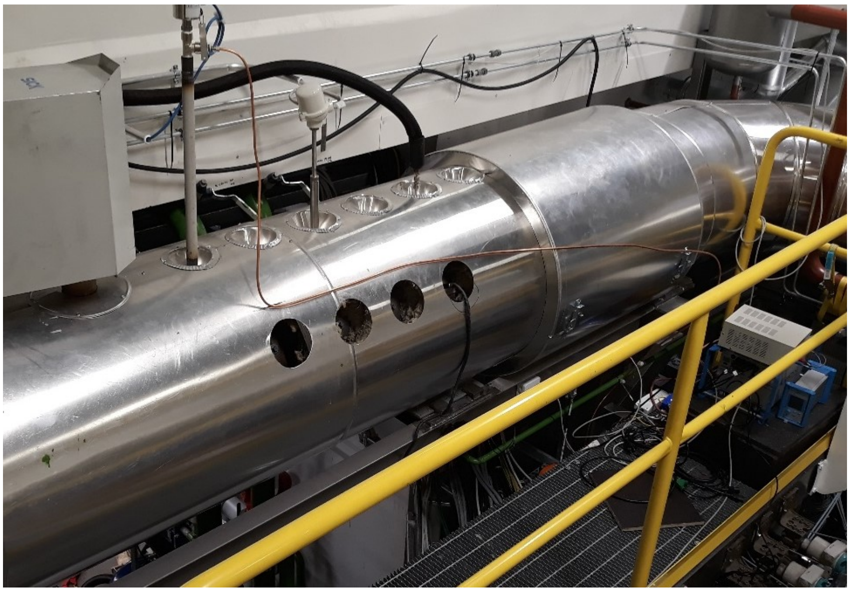

Figure 5. The exhaust gas sample measuring points. Altogether six spots and some instruments are located on top of the exhaust pipeline.

Figure 6. The sample measuring point with the capped nut removed.

The schedule for both engine runs is presented in Table 9. The discrepancies between the load increasing points are quite significant. The rough plan was to run the engine at three different load points: 0 %, 25 % and 50 %. Footage would be gathered throughout the test to see any possible discrepancies. The last measurement point would be taken 50 minutes after the exhaust gas pipeline had become visibly warm.

Only the engine run without artificial leakage ended up following the original load plan. Furthermore, the engine was operated considerably longer and at additional load points compared to the reference case. The video material produced with artificial leakage after load point 50 % was disregarded from the comparison.

Table 9. Engine load points and timestamps for the experiments.

	No leakage 27.11.2019		**Artificial leakage 28.11.2019**	
Command	Timestamp	From engine start	Timestamp	From engine start
Start, idling	10:56:48	00:00:00	12:35:01	00:00:00
Load 25 %	11:15:11	00:18:23	13:01:36	00:26:35
Load 50 %	11:28:53	00:32:05	13:15:43	00:40:42
Load 75 %			13:29:28	00:54:27
Load 100 %			13:38:30	01:03:29
Load 0 %	11:55:22	00:58:34	13:48:57	01:13:56
Shutdown	12:06:37	01:09:49	14:04:13	01:29:12

The second comparison was made with fixed time interval, disregarding the slight discrepancies between the schedules. The assumption was that given enough time, the heat profiles on both situations would even up, except for the area where artificial leakage is induced. A 50-minute timer was started from the point when any visible change in the IR video material could be seen. The material would then thoroughly be inspected to find evidence of the produced leakage.

3.3.2 Before the turbocharger

By using the same rail as in the previous experiment, the thermal camera was repositioned and pointed towards the engine (Figure 7). In this experiment, the artificial exhaust gas leakage was produced in the engine's internal exhaust system before the TC. At this stage, the exhaust gas temperature is much higher compared to the sample measuring point, making it easier to detect.

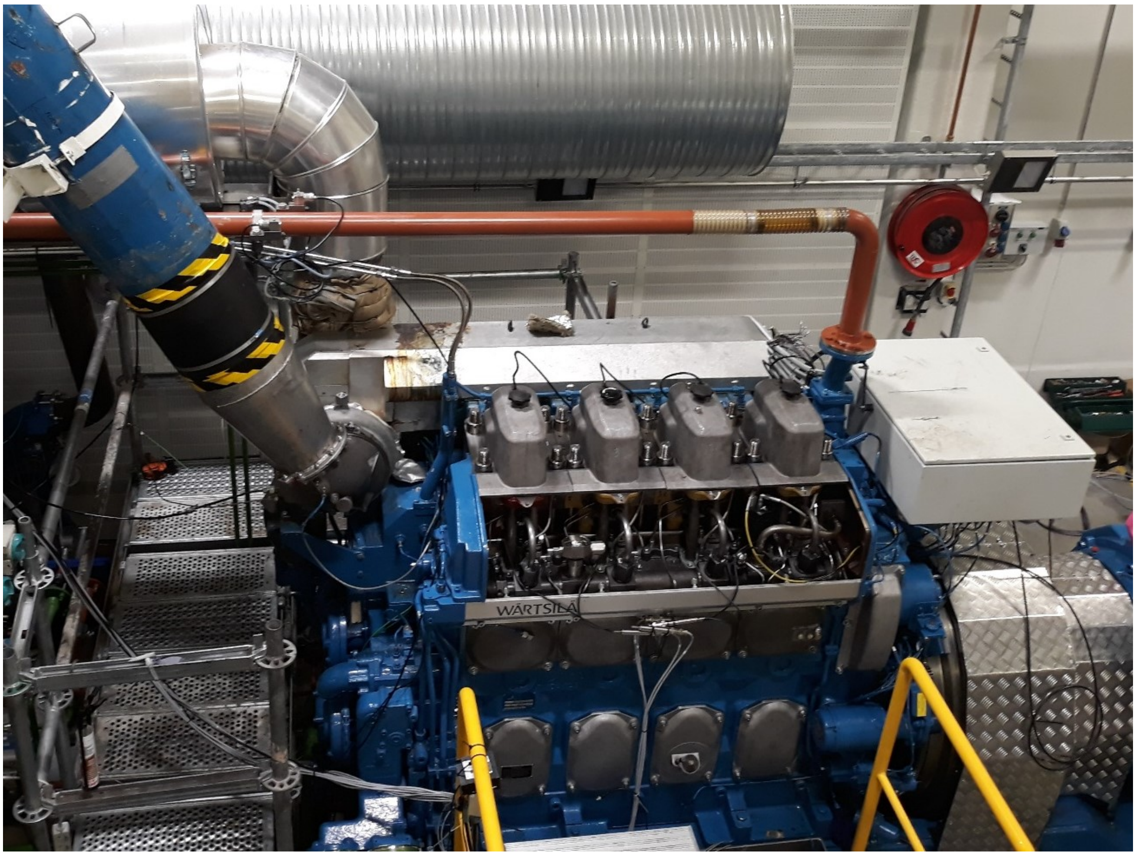

Figure 7. The engine as seen from the thermal camera.

The leakage was produced by removing one of the tubes leading to a free-flow pressure sensor (Figure 8). The second pressure sensor's tube was left intact to get a reading on the pressure level before the TC. There are no clear targets for the exhaust gas stream to collide into, but the edges of the nozzle should reach higher temperatures compared to a situation where the tube is attached.

Figure 8. A closeup of the exposed connector to the engine's internal exhaust gas system, circled in red.

Due to high discrepancies between the load increase timestamps in the previous experiment, a schedule was produced for better uniformity to the engine runs (Table 10). Nonetheless, the schedule is more for guidance to the engine operators than a strict rule set: the engine load ramp up is limited by the exhaust gas and in-cylinder temperatures. After all, these experiments were not meant to push the physical limits of the engine. A safe and steady approach was applied throughout.

Table 11 shows the final engine run schedule. Discrepancies between the engine runs are now significantly smaller, but still present. The commands for ramp-down and shutdown are also presented, which were completely lacking from both the previous experiment and the planned schedule. All in all, the experiment's engine runs were acceptable for producing material for situations with and without an exhaust gas leakage.

Table 10. Planned engine run schedule for the second test.

Command	**Time**
Start, idling	00:00:00
Load 25 %	00:15:00
Load 50 %	00:20:00
Load 75 %	00:25:00
Load 100 %	00:30:00

Table 11. Engine load points and time stamps for the second leakage experiment.

	No leakage 3.3.2020		**Artificial leakage 4.3.2020**	
Command	Timestamp	From engine start	Timestamp	From engine start
Start, idling	12:25:26	00:00:00	10:06:03	00:00:00
Load 25 %	12:42:56	00:17:30	10:22:58	00:16:55
Load 50 %	12:49:30	00:24:04	10:29:07	00:23:04
Load 75 %	12:57:11	00:31:45	10:34:54	00:28:51
Load 100 %	13:05:13	00:39:47	10:40:45	00:34:42
Load 50 %	13:20:54	00:55:28	11:02:11	00:56:08
Load 0 %	13:29:15	01:03:49	11:12:41	01:06:38
Shutdown	13:37:40	01:12:14	11:21:36	01:15:33

This experiment was repeated the second time to produce additional video material for the ML validation analysis. The realized timetable from the previous experiment (Table 11) was utilized and the engine was run at each load point as close to the original schedule as possible. Table 12 presents the actual timestamps and the time difference between each load point compared with the previous engine run. The differences between running times in these experiments were generally low, with most differences being under 10 seconds. However, some outliers with higher running times were also present. Due to the method of presenting these values, it has to be noted that the second experiment resulted into cumulatively longer running time compared with the first dataset, but only slightly.

Table 12. Engine schedules for the repeated experiment. Differences in how much longer or shorter time the engine was driven at a specific point compared with the previous engine runs.

	No leakage 16.3.2020		**Artificial leakage 12.3.2020**	
Command	Timestamp	Difference	Timestamp	Difference
Start, idling	09:47:03	00:00:17	12:19:32	00:00:14
Load 25 %	10:04:50	00:00:05	12:36:41	00:00:27
Load 50 %	10:11:29	00:00:00	12:43:17	00:00:03
Load 75 %	10:19:10	00:00:03	12:49:07	00:00:03
Load 100 %	10:27:15	00:00:10	12:55:01	00:00:06
Load 50 %	10:43:06	00:00:12	13:16:33	00:00:06
Load 0 %	10:51:39	-00:00:02	13:27:09	00:00:22
Shutdown	11:00:02		13:36:26	

3.3.3 Machine learning

The produced IR video materials on both experimental setups were used to train and detect the induced leakage with the help of ML algorithms. The work on this task was done by the project partner Top Data Science. All the thermal video material was produced with the ML aspect in mind. In essence, all other variables except the leakage were attempted to be as close to similar as they were in reference engine runs. As a result, the ML algorithms should reliably be able to detect between no leakage and leakage situations (N. Säkkinen, personal communication, March 10, 2020). Different tools were applied in trying to detect the leakage either locally, at the site of artificial leakage or globally from the footage.

For the first experiment, the complete IR footage from both cases were used to train the ML algorithms to distinguish between leakage and no leakage cases. The same material was then back tested to see if any distinction can be made.

For the second leakage experiment with more abundant footage, the earlier parts of the IR footage were used for training purposes. The latter parts were used to validate the algorithms. However, repeating the second experiment allowed using the complete engine run material from one experiment to be trained and tested on the material from the other experiment.

3.4 Utilizing existing signals

During the engine test runs, the Adlink did not possess software to reliably log any critical engine data. Instead, the data was already being stored by Labtool. Unfortunately, using the Adlink to read data from Labtool was not possible. Therefore, the data needed to be manually transferred. This was achieved by using an external storage device.

The Labtool dataset was first filtered to get the correct data points. Then the data feed range was set to only include the timestamps around the experiments. With this data storage method, one hour of engine run corresponds to approximately 30 MB of plain .csv data. After completing the data transfer to Adlink, it was further transferred to the AWS S3 bucket for long term storage.

With the gathered data from several engine runs, the company partner Edupower built a neural network (NN) with the task of predicting engine vibration levels. Four engine runs were used to train the NN and one engine run to test it. The most distinguishable frequencies were selected based on FFT observations. The model used 113 individual signals to build a baseline on vibration level development with signal input variation. The network produced a total of 79 output values. (A. Korsbäck, personal communication, January 28, 2021).

4 Results

This section presents the results for the vibration sensors' performance, exhaust gas leakage detection and the existing signals. For vibration sensors, the data was gathered from as many engine runs as possible. The exhaust gas leakage detection experiments were more focused and fewer. Other engine data was gathered and inspected during the trials.

4.1 Vibration sensors' performance

Rather than presenting several series of raw or manipulated vibration data, these results are focused on the experiences with this type of sensor set-up and installation locations. The raw data was monitored and stored. However, as the main task was demonstrating the system in a laboratory environment before the implementation in a real vessel, the focus was set on detecting the weaknesses and solving potential issues that could arise when the system is out of reach.

Among the first things that required attention was data handling: internal storage filled up very fast, resulting in changes with data management. One vibration sensor was producing approximately 500 MB of data each day and it was all stored locally. As a result, 1 TB external solid-state drive was attached to the system to handle all the remaining data for the duration of the project.

The cloud storage was handled differently to only include data from the days the engine has been running. A. Lundell (personal communication, February 2, 2021) describes the method the following way: a script was developed to combine the data from x, y and z axes on a specific day. The variances in the combined data are checked to deduce if the engine has been on. If the variances are high enough, the data is uploaded to the S3 cloud bucket. The script did not run automatically every day, but had to be manually initiated.

After one critical update to InfluxDB, fatal issues for vibration data processing appeared. The FFT calculations could not get going. The solution for this issue was to install a Raspberry Pi to handle the calculations. Unfortunately, one Raspberry Pi could not handle the data pre-processing for two 500 Hz signals. In response, the vibration FFT rate was dropped down to 400 Hz solving the issue (A. Lundell, personal communication, December 3, 2020). The raw data was still stored at 500 Hz, but the FFT was done at 400 Hz rate for both sensors.

Lastly, the system suffered from minor stability issues. The internal clock's of vibration sensors could drop out from synchronization, which had to be solved by a reboot. In some cases, the vibration sensors stopped working while in the middle of an engine run, causing loss of vital data. The later installed Raspberry Pi which solved the data processing issues kept having complications with stability.

4.2 Exhaust gas leakage detection

The results for exhaust gas leakage detection are presented with still frames at key timeframes from the produced thermal video material. A side-by-side comparison between the experiments without and with leakage are presented for each case.

4.2.1 Exhaust gas pipeline

The first still frame from the exhaust gas pipeline experiment was taken when starting the engine (Figure 9). A faint glow is visible on the exhaust gas pipeline in both cases. The frame on the right appears universally bluer, i.e. warmer, in comparison with the frame on the left. A faint glow appears in the holes made to the thermal insulation on the right frame. The hottest spots in both frames appear to be around 50 to 60 °C.

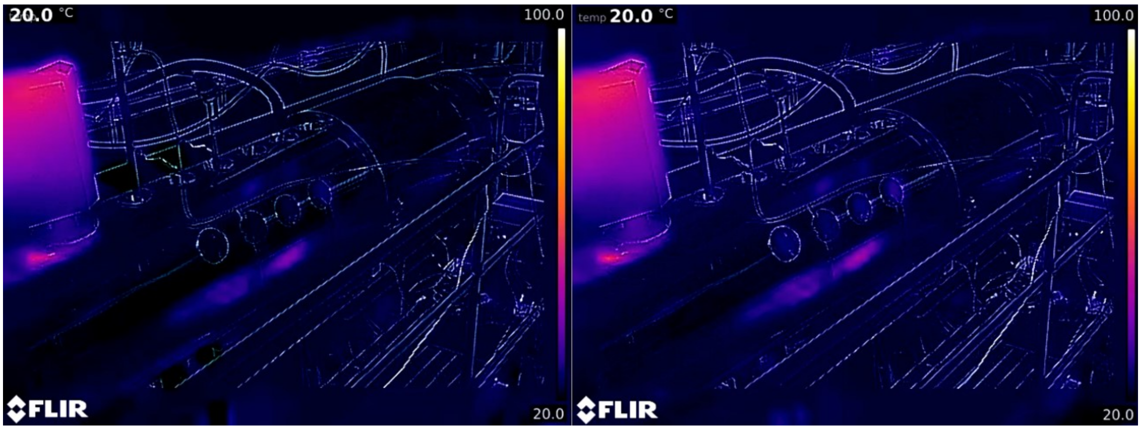

Figure 9. Temperature when starting the engine. No leakage on the left, artificial leakage on the right.

After the engine had been ramping up via different load points and thermal levels balanced, a new comparison was made 10 minutes after the load command to 50 %. Figure 10 shows a frame of the thermal video. As before, the glow on the side of the exhaust gas pipeline is visibly brighter on the right. The temperature in the holes of the thermal insulation exceed well above the scale in both situations. Around the artificial leakage site, the frame on the right appears more brighter than on the left. However, that applies on the whole frame in general.

Figure 10. Temperatures 10 minutes after the load command to 50 %. No leakage on the left, artificial leakage on the right.

A second inspection of the footage with slightly different time stamps was performed. After timestamps 10:58:49 and 12:36:54 for no leakage and leakage situations respectively, the exposed exhaust gas pipe shows first signs of heating up (Figure 11). After 50 minutes had passed, new frames were taken and the results compared with the initial footage. Other remarks on the differences between frames in Figure 11 are similar to Figure 9: a slightly brighter glow on the side of the exhaust gas pipeline and universally bluer frame. At this stage, there are no visual clues suggesting the existence of exhaust gas leakage on the right frame.

Figure 11. Signs of heat visible in the cut-outs on thermal insulation. No leakage on the left, artificial leakage on the right.

50 minutes past after the first signs of heating up corresponds to timestamps 11:48:49 for the experiment without the leakage and 13:26:54 for the experiment with the artificial leakage. These frames are presented in Figure 12. The results are similar to previous observations: a brighter glow on the side of the exhaust gas pipeline and universally bluer or purple fade on the right frame. No evidence of the artificial leakage can be detected.

Figure 12. Temperatures 50 minutes after the exhaust gas pipeline had started heating up. No leakage on the left, artificial leakage on the right.

To ensure that the expected heating effect does not occur faster than anticipated, a comparison during the load command to 25 % was performed. At this stage, the cut-outs are visibly heated (Figure 13). The highest temperature points range from 90 °C in the left frame to 100 °C on the right frame. Otherwise, similar remarks as with other comparisons are present. No visible changes that could indicate a leakage can be seen in the artificial leakage area.

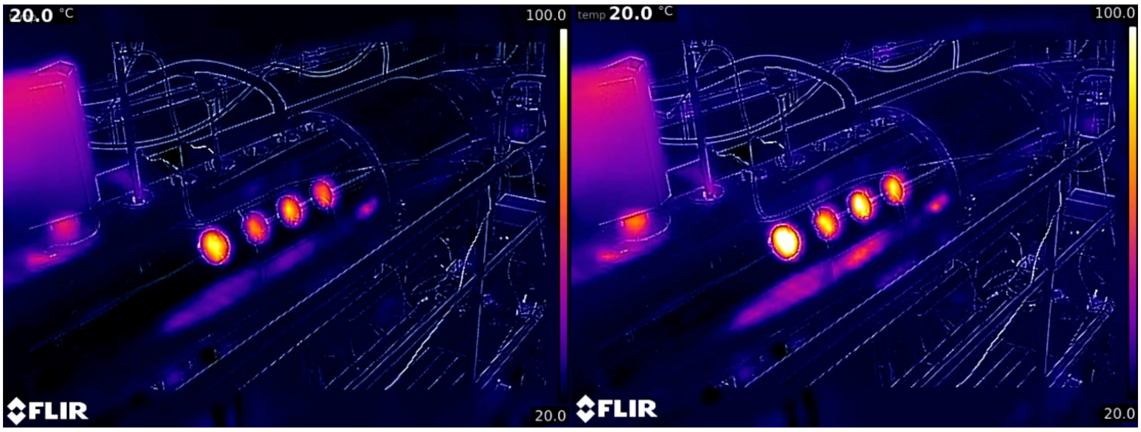

Figure 13. Temperatures at the load command to 25 %. No leakage on the left, artificial leakage on the right.

Training the ML algorithms first with the IR video materials and back testing of both videos resulted in the algorithm recognizing the correct situation with over 99 % confidence interval. However, there was a substantial bias between the produced video materials: the blue glow present during the whole engine run in the artificial leakage situation. Additional video footage would be needed to deduce if the leakage can be detected with ML tools or not.

4.2.2 Before the turbocharger

The first attempt with this set-up resulted in a failure. The engine had to be shut down due to a faulty injector in cylinder 4 on February 2nd 2020 (Table 8). It was caused by a minor electric fault and was quickly repaired. After a successful engine start-up test on the next day, the engine was ready for another attempt with artificial leakage experiments.

The second attempt was successful. During the time when the engine was started, there were slight noticeable differences between the frames (Figure 14). The frame on the right shows that the engine is slightly more heated up compared with the frame on the left. Additionally, there is slight visible change in the leakage area caused by the removal of one of the pressure sensor tubes. A piece of loose insulation sits on top of the engine in the frame on the right. The top of the frame is somewhat bluer in the frame on the right. The hottest spots in both frames appear to be around 50 to 60 °C.

Figure 14. Temperatures when starting the engine in the second experiment. No leakage on the left, artificial leakage on the right.

After full load was achieved and the temperature levels in the engine evened out, a new inspection of the engine was taken (Figure 15). The whole area around the TC is completely bright, indicating temperatures exceeding well above the maximum 100 °C scale. The area around the leakage has a hotter heat profile on the right. Otherwise, the heat profiles of the engine are almost identical in both frames. However, a pipeline in the top of the picture appears hotter in the frame on the right.

Figure 15. Temperatures 10 minutes after the load command to 100 % in the second experiment. No leakage on the left, artificial leakage on the right.

To see if there is a clearer distinction around the leakage area at lower loads, the footage was again investigated at the load command to 25 %. In Figure 16, the higher heat signature from Figure 14 is still visible on the engine in the right frame. Interestingly, the heat signature around the artificial leakage appears hotter in the left frame. There is no indication that the leakage would be induced on the right frame at this stage.

Zooming in the leakage area, a noticeable pattern starts to emerge after the command to the load point of 50 % (Figure 17). The frames with the induced artificial leakage are clearly sending a stronger heat signal. The signal is either miniscule or non-existent at loads below of 50 % when starting the engine.

Figure 16. Temperatures at the load command to 25 % during the second experiment. No leakage on the left, artificial leakage on the right.

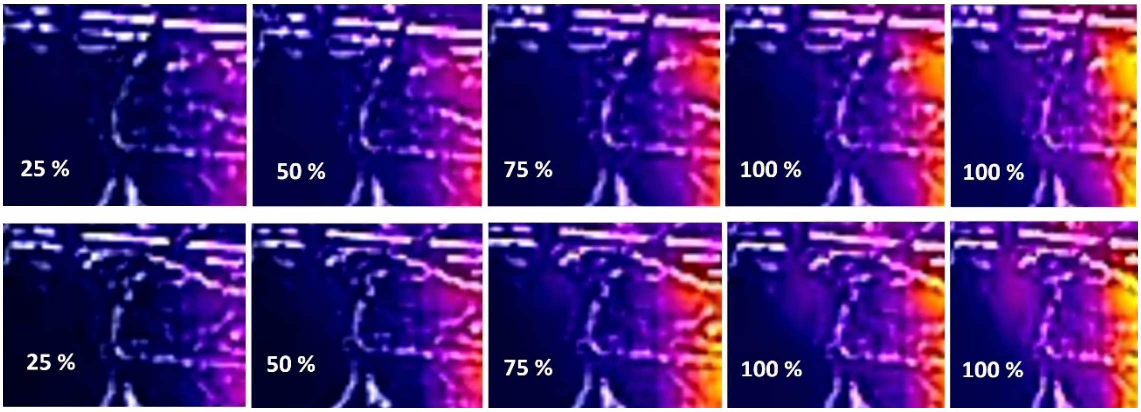

Figure 17. Artificial leakage area at different load command points in the second experiment. No leakage (first row) versus artificial leakage (second row). The last frame is taken 10 minutes after the load command to 100 %.

N. Säkkinen (personal communication, March 17, 2020) explains that the ML tools were used to train the dataset on the first 75 % of the material. The last 25 % of the footage was used to validate the algorithms. They were successfully able to identify the correct situation from 69 % to 100 % time depending on the used feature descriptor. However, additional validating experiments concluded that the identifying factor is most likely caused by other variables, such as slight differences in the camera angle and in the heat signatures on the whole frame.

The exhaust gas leakage experiment was repeated a third time to gain additional material for ML analysis. This time the overall heat signal was distinctly stronger in the frame without the artificial leakage (Figure 18). There heat detected by the camera from the pipeline above the engine is very minor in both frames. However, a rack has been installed behind the engine between this and the previous experiment. It is clearly visible as a rectangular shape close to the top of the engine. The leakage area is marginally different due to the tube removal explained before. The hottest parts in the engine are around 50 °C.

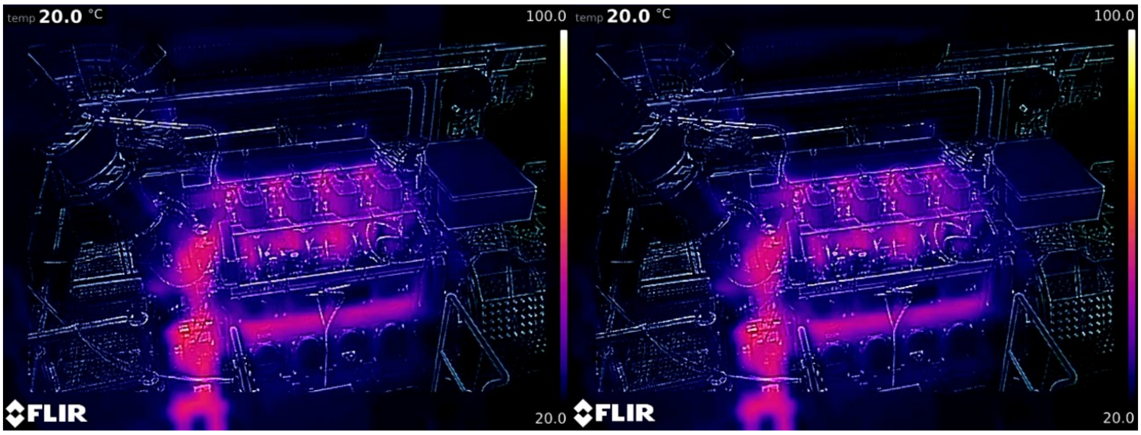

Figure 18. Temperatures when starting the engine in the third experiment. No leakage on the left, artificial leakage on the right.

After the engine was fully heated up and been running for 10 minutes since the full load command, a comparison was made. In Figure 19, the overall heat signal of the engine is very similar between the two frames. The heat coming from the pipeline above the engine is even in both frames, more than in the second experiment (Figure 15). The area around the induced artificial leakage generates a stronger heat signal than in the frame on the left. A slight glow can be registered from the newly installed rack in the top right part of the engine.

Figure 19. Temperatures 10 minutes after the load command to 100 % in the third experiment. No leakage on the left, artificial leakage on the right.

Backtracking to 25 % load command while the engine is still ramping up, the same characteristics as existed in Figure 18 are still visible (Figure 20). The hottest parts of the engine appear to be around 60 °C, with a slightly hotter appearance on the left frame. While comparing the areas around the TC, the frame on the right emits a stronger heat signal. There is no clear sign of the exhaust gas leakage in the right frame.

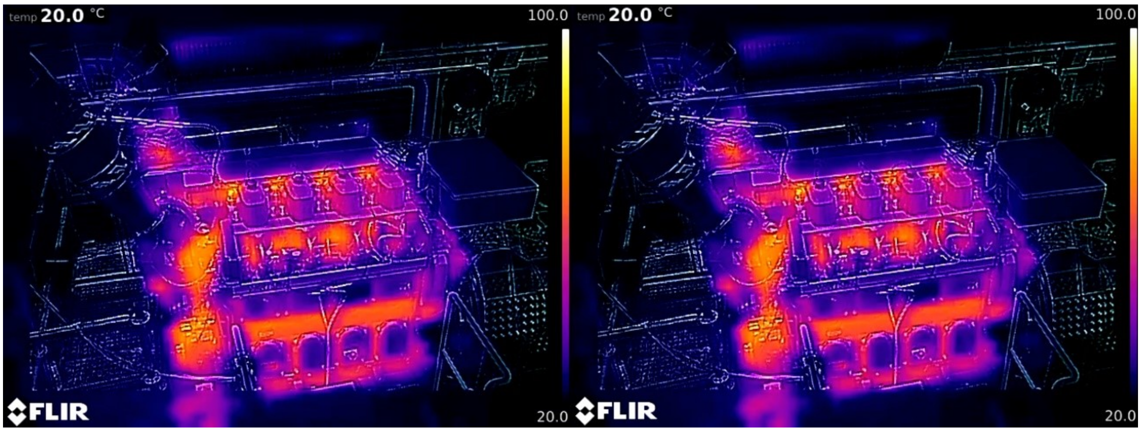

Figure 20. Temperatures at the load command to 25 % during the third experiment. No leakage on the left, artificial leakage on the right.

With a closer inspection on how the heat map around the artificial leakage area develops at different load points, the results in this experiment share a mutual pattern with the second experiment (Figure 21). The heat signature with the induced artificial leak is stronger, and the difference visible from load command to 50 % onward. After starting up the engine and idling, the difference is very minimal or unnoticeable.

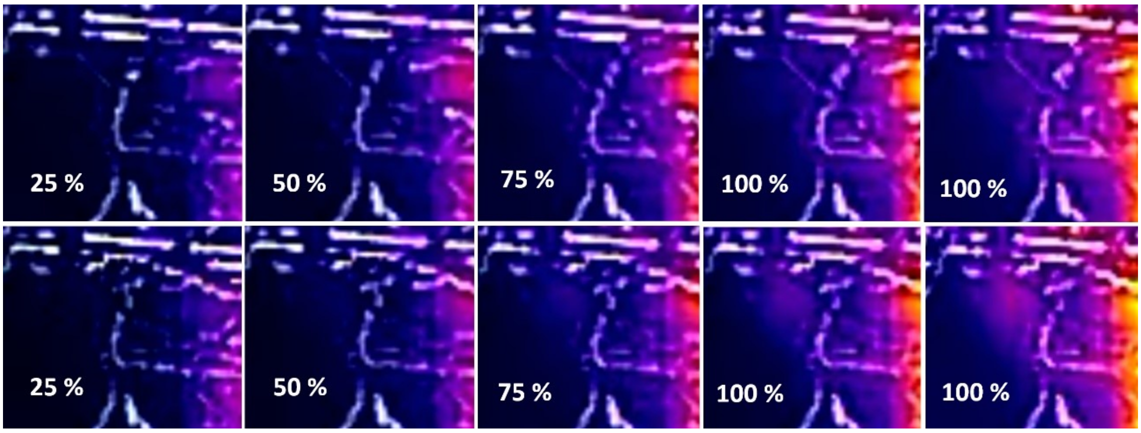

Figure 21. Artificial leakage area at different load points while ramping up in the third experiment. No leakage (first row) versus artificial leakage (second row). The last frame is taken 10 minutes after the load command to 100 %.

To see how the pattern evolves when load is decreased, new visual data that was absent from the previous experiment is presented. Figure 22 shows how the heat signal with the artificial leakage persists, but diminishes in strength. The heat signal from the area without the artificial leakage has a slight decrease while ramping down.

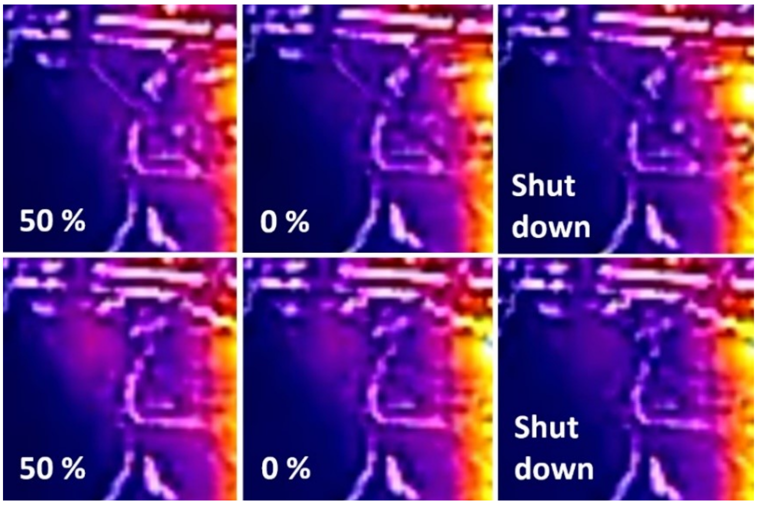

Figure 22. Artificial leakage area at different load points while ramping down in the third experiment. No leakage (first row) versus artificial leakage (second row).

Since the IR video footage cannot be used to estimate the temperature of the exhaust gas as it is leaking, the temperatures at different load points were recorded. This occurred just before moving to the next point in the engine run schedule. The temperatures are presented in Table 13. The trend between the exhaust gas temperature and engine load is distinct.

Table 13. Engine load and the temperature range for the exhaust gas before the turbocharger.

Timestamp	Load	Exhaust gas temperature
10:04:00	Idling	235 – 259 °C
10:10:40	25 %	400 – 424 °C
10:18:20	50 %	455 – 479 °C
10:26:25	75 %	480 – 500 °C
10:42:10	100 %	519 – 547 °C
10:50:40	50 %	451 – 493 °C
10:59:15	0 %	270 – 303 °C

The additional produced IR footage was used for a new set of ML algorithm experiments. N. Säkkinen (personal communication, March 24, 2020) describes the methodology and results: the data from second experiment was used to for training purposes and the third experiment data was used for model verification. The whole frame of the video was not utilized, only specific areas of the engine locked by bounding boxes were used for training and validation. The results indicate that the used methodology could not distinguish between leakage and no leakage cases, with accuracy around 40 – 60 %.

N. Säkkinen (personal communication, March 24, 2020) further developed the training and testing method, cropping the used bounding boxes randomly by ten pixels. This method additionally diminishes the effect of slightly different camera angles between training and validation data sets in both experiments. The random cropping resulted in improving the accuracy to 85 % for the bounding box hosting the leakage area. In other bounding boxes the accuracy ranged between 40 – 50 %.

However, the proceeding measures for validating whether the results are in fact caused by the leakage and not by any other possible bias abused by the training algorithm showed mixed results. Therefore, the conclusion was that with the selected ML methods and available data, the artificial leakage could not be reliably detected universally from the video material. To resolve the matter, additional datasets would be needed to rule out the possible biases in the selected classifier. The biases include preheating, load differences and the camera angle. (N. Säkkinen, personal communication, April 22, 2020).

There was a desire and plan to produce additional IR video material to resolve the issues described above. Unfortunately, no new data could be produced after March 16th 2020. The engine had to go through a testing period, with changing parameters that could jeopardize the consistent running schedule. Other unfortunate limitations were caused by COVID-19 restrictions, reducing the allowed research personnel in the control room and thus challenging the ability to conduct any other experiments.

4.3 Existing signals

The manual data collection and transfer method prevented the ability to apply edge computing and real time data analytics. Nevertheless, due to the data requirements for establishing a baseline for operational behaviour, the work in this aspect was not wasted. The company Edupower presented results for a NN experiment using four separate engine runs as training data for vibration level predictions. The results are discussed on general level in this section.

The model showed promising results. It correctly predicted both the amplitude of vibrations with acceptable margins for most of the time. However, when ramping down the engine and idling, the model consistently predicted higher than measured vibration levels in almost all simulated frequencies. Ramping up and running at steady load produced more accurate results. (A. Korsbäck, personal communication, January 28, 2021).

5 Discussion

This section explores the validity of the produced results, and their implications in further detail. Improvements to the test set-ups are suggested. In addition, topics that need to be addressed in potential future work are brought up.

5.1 Vibration sensor performance

Despite the performance issues reported in section 4.1, the vibration sensors managed to fulfil their task as a demonstrator for the final system setup installed in the engine room of an operating vessel. The used sensors are rated for IP 30, which limited the positioning to further away from the cylinders in fear of damage from potentially spilling engine oil. Additionally, the vessel installation could not use Wi-Fi connection for data transfer. This led to building a custom vibration sensor package with protective casing and cable connections to the edge devices. The resulting device used the same vibration sensor included in the Bosch XDK110 and could be installed closer to the cylinders. Stability issues were solved by updating the XDK110’s software to boot itself every night. This reduced the chance for both of them crashing simultaneously.

One aspect completely lacking from the vibration data analysis is the data comparison to high performance vibration sensors. There was a general interest to collect data with piezoelectric sensors from the engine to validate the seen vibration levels. As adequate equipment did not exist in the laboratory facilities, a plan to borrow a high-performance analyser was made. Unfortunately, COVID-19 restrictions combined with long maintenance breaks with the engine (Table 8) towards the end of the project completely voided the plans. In any future development, this issue should have a high priority.

Development happened in the aspect of data handling. As the internal storage got filled up, an additional external hard drive was installed. The final edge computing device should not need tremendous amounts of storage, as the data would be monitored for specific nuances, or the lack off. During the duration of the project, there was not enough data gathered to know when the engine was running completely normally, or if the vibration levels are developing into a stage indicating oncoming component break down.

Building a vibration baseline for the laboratory engine is arguably more challenging compared with a conventional marine engine. Over the years, the engine has gone through various changes to its parts, with the standard parts replaced by custom-made and experimental ones without proper existing documentation. Building a well-trained NN for engine fault prediction would serve only for the experience in building one, as the resulting vibration baselines might not be completely applicable to other existing engines. Jimenez et al. (2020) worked with 15 515 measurements, covering a wide range of possible situations for their condition monitoring models. By contrast, a total of 51 engine runs were conducted with vibration data successfully gathered from 43 engine runs.

5.2 Exhaust gas leakage detection

Both conducted exhaust gas leakage experiments suffered from shortcomings that affected the perceived results. In the first test setup, the outpouring exhaust gas jet failed to properly hit any surface close to the leakage site. There was also a concern that the exhaust gas is not hot enough to meaningfully heat the surroundings. Additionally, any attempts to directly detect the exhaust gas jet with wavelengths visible to the eye from the distance of the camera were futile. Even the human eye could not detect any leakage standing at the position of the camera. The leakage was visible only when standing next to it on the pathway visible in Figure 5.

In addition to issues in the test setup planning, there were other nuances regarding how the engine was run that required attention. As it was first thought that the possible differences in temperature around the leakage site would be rather easily detectable, the initial plan merely included load points up to 50 %. When it was time to induce the exhaust gas leakage and observe the results, it became evident that one could not immediately distinguish between the two cases. The original load schedule was scrapped and the load increased up to 100 % (Table 9). Even though the IR video material after load points 50 % were excluded from comparison, the difficulty for a human observer to detect any evidence of the leakage from the footage at full load meant that changes had to be made to the test setup.

Smaller issues related to inconsistencies in the engine preheating and having a more similar ramp up times between the experiments were also noted. A rather surprising remark came from the differences in the heat signatures that can be seen before the engine has even started (Figure 9). Two possible explanations are presented for this. Either the automatic adjustments inside the thermal camera caused the perceived colour scale to slightly shift between the experiments, resulting in everything looking slightly hotter than in the engine run day before, or the temperature in the laboratory and in the exhaust gas pipeline was slightly warmer during the second engine run. Slight differences in the temperatures in Figure 14 compared with Figure 18 would suggest the latter to be true, as the experiments in Figure 14 were conducted during successive days. Engine runs between experiments in Figure 18 had a few days in between and showed no difference between heat signatures around the surroundings.

All the described factors resulted in changing the experiment setup completely, planning a better engine run schedule and increasing the maximum load point from 50 % to 100 %. Thus, the second exhaust gas leakage setup was better planned and executed. Unfortunately, not all factors described above could be improved. The engine pre-heating was inconsistent between the experiments, as proved by the heat differences on the engine before starting up. Original schedule was slightly deviated from and did not include the plan for ramping down, which developed while running the engine for the first successful attempt on the second setup. Despite small discrepancies between the engine runs, the produced load schedule was followed as accurately as possible. This can be noted especially well on the retake of the second experimental setup, which had almost identical schedule compared to the previous engine runs. Only the information of the exhaust gas temperature at various load points were added to the schedule.

Based on two different test setups, it can be deduced that exhaust gas leakages cannot be directly detected with a conventional thermal camera. However, as proven by results in Section 4.2.2, the leakage can be indirectly detected under the right circumstances. From the first test setup, the leakage signal was either too weak or non-existent to be noticed. Under the second test setup, the exhaust jet directly made contact with the scaffolds supporting the exhaust gas pipeline, barely visible in Figure 7. The scaffold and the dark grey part are better presented in Figure 23. The camera position could have been changed to better see behind the duct for charge air intake, but due to the ML analysis and the desire to not change anything in the setup, no adjustments were made.

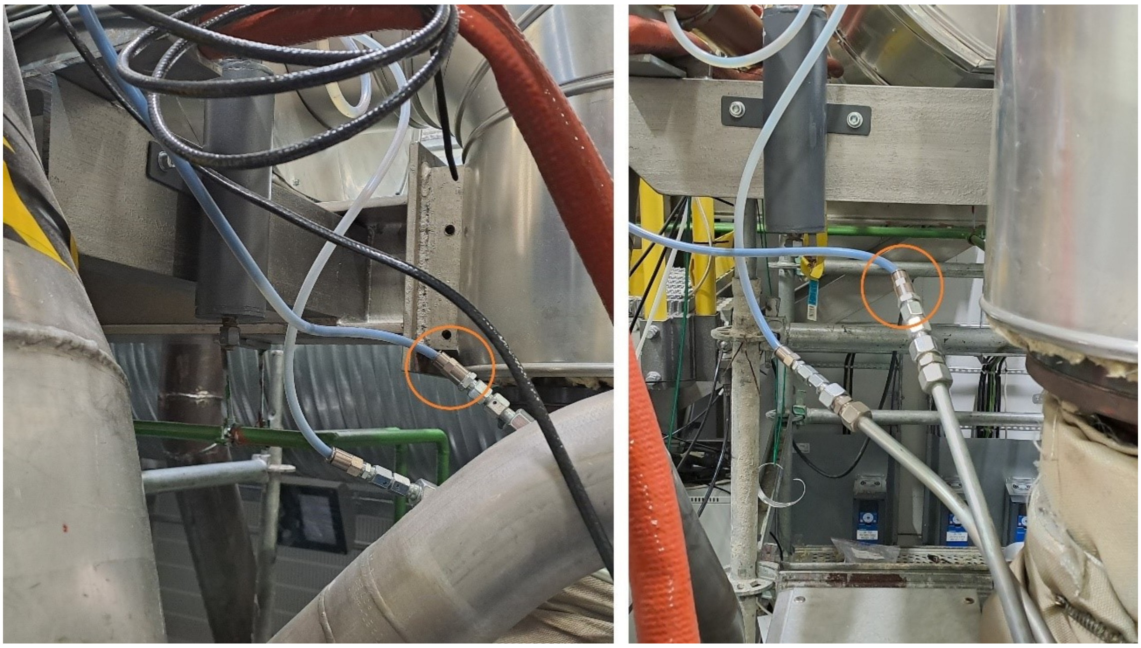

Figure 23. The source of artificial leakage from two different angles.

The results reveal another critical matter from the aspect of leakage detection and that is the lag. When the engine is ramping up, the heat difference can first clearly be seen after loads from 50 % onwards (Figure 17 & Figure 21) when the engine has been running for over 20 minutes. The signal becomes stronger at higher loads, with the higher exhaust gas temperature being a significant factor contributing to the detection. When decreasing the load (Figure 22), the heat signature lingers longer and is still visible after 10 minutes of idling and shutting down the engine.

There is very little research in using thermal cameras for detecting exhaust gas leakages. Thermal cameras have been used for rotating machinery condition monitoring (Bagavathiappan et al., 2013) and as a method in order to detect gas leakages from pipelines (Jadin & Ghazali, 2014), but the experiences with internal combustion engines is very limited. Counter to transferring pressurized natural gas in an exposed pipeline which cools the surface around the leakage area due to fast density change (Nawrat et al., 2012), the expected effect on a leaking exhaust gas pipeline is the opposite. This is due to the insulation layer surrounding the hot exhaust gas pipeline and a low pressure difference between the pipeline and surroundings. Given enough time, the additional heat released by leaking exhaust gas should provide a higher heat signal compared with status quo. This aspect should be further researched, as the ability to remotely pinpoint the approximate location of a leakage while covering a large area is a compelling argument.

Detecting leakages with thermal imagery has additional weaknesses, that can be listed. Several thermal cameras might be required to cover all the possible angles for comprehensive leakage coverage, increasing the price tag for such a system. Additionally, there is a risk that a small leakage goes unnoticed for extended periods, if the temperature differences around the leakage area is small. Other sensing methods should be applied in parallel to solve this issue.

Even though the ML algorithms could not unquestionably distinguish between the different leakage scenarios, the definite answer would have been got after a few new successful leakage experiments. After final results, the experiment setup could be further developed to increase the chance of detecting the leakage. Such methods are changing the camera position, using pure IR video feed for recording, changing the scale to properly see small nuances in the recorded temperature and using more dynamic engine runs for ML training.

5.3 Existing signals

Setting the baseline operational ranges for each individual signal covering every possible situation requires enormous amounts of collected data and good data handling tools. The latter part was covered during the project, but the amount and the way data needed to be transferred limited its potential. This issue was deeply noted and later on resulted in a complete overhaul for the data collection system used in the laboratory.

Similarly, the NN results presented by Edupower were promising, but only scratched the surface. Even without combining the engine basic operational data with measured vibration data, Jimenez et al. (2020) showed how predictive maintenance models for vessels can be built. It is recommended to keep storing engine operational data in perpetuity, as more advanced models will be built over time. For that reason, every bit of data counts.

6 Conclusions

In this thesis, the task was to build an edge computing platform to be tested in a laboratory environment. The knowledge and experiences would be used to further develop the system and install it in an operating vessel. Two edge computing devices were installed to handle vibration data gathered from a marine engine. Additionally, thermal imagery was utilized for exhaust gas leakage detection. Regular engine operational data was collected and stored for condition monitoring purposes.

As a result of the conducted work, the following conclusions could be made:

- An edge computing system was successfully built and demonstrated. The system allowed for remote supervision of the vibration levels produced by a running engine.
- High priority should be placed on system stability. Small issues can easily be solved in the laboratory, but remote operation requires robustness.
- Exhaust gas leakages can be indirectly detected with a thermal camera, if the correct conditions are met.
- The visible heating effect from the exhaust gas can only be seen over extended periods of time or at higher engine loads.

Based on the conclusions above, the following recommendations can be made:

- Industrial grade hardware should be used from the sensors to the edge computing device.
- If a thermal camera is used to detect exhaust gas leakages, it’s sensitivity scale should be properly calibrated for unexpected heat signals.
- Because the exhaust gas leakages can be detected by a human observer from the thermal camera, the ML algorithms for leakage detection must further be developed.
- If fast and reliable exhaust gas leakage detection is required, other detection methods should be weighed.

7 Summary

The VEBIC laboratory system was introduced as a demonstrator for edge computing. This included the already existing equipment and tools available as well as the new hardware and software purposefully acquired to conduct the research. An edge computing set-up with vibration sensors was built, using easily accessible hardware and software to tackle potential issues that could arise if the system were installed on an operating vessel. Additionally, research was conducted whether a regular thermal camera could be used to detect exhaust gas leakages. Regular engine data was gathered throughout the experiments in order to include it in the edge computing platform.

The edge computing system was successfully demonstrated, allowing vital processed vibration data to be viewed remotely. The system consisted of two vibration sensors wirelessly connected with two edge computing units. As a result of this work, the foundation for engine condition monitoring with a vibration baseline model has been set. The experiences with the system note that extra attention should be given to system stability and robustness.

Based on the results in this work, exhaust gas leakages can indirectly be detected with a regular thermal camera. The detectability increases with engine load and has a lag in response to the load, but is generally weak. However, the ability to remotely detect and approximate the location of an exhaust gas leakage is an advantage. Therefore, this method should be further researched on.

Sources

Aasen, G. (2017, September 22). *Introduction to InfluxData as InfluxDB and TICK Stack*. InfluxData. Accessed 17.8.2023 from https://www.influxdata.com/blog/introduction-to-influxdatas-influxdb-and-tick-stack/

Adlink Technology. (2013). *MXE-5400 Series*. Adlink Technology, Inc.

Bagavathiappan, S., Lahiri, B. B., Saravanan, T., Philip, J., & Jayakumar, T. (2013). Infrared thermography for condition monitoring – A review. *Infrared Physics & Technology*, *60*, 35–55. https://doi.org/10.1016/j.infrared.2013.03.006

Bosch. (2016). *Cross-Domain Development Kit XDK110*. Bosch Connected Devices and Solutions GmbH.

CentOS. (n.d.). *About CentOS*. Retrieved September 5, 2023, from https://www.centos.org/about/

InfluxData. (n.d.-a). *Kapacitor*. InfluxData. Retrieved September 1, 2023, from https://w2.influxdata.com/time-series-platform/kapacitor/

InfluxData. (n.d.-b). *Telegraf*. InfluxData. Retrieved September 1, 2023, from https://w2.influxdata.com/time-series-platform/telegraf/

Jadin, M. S., & Ghazali, K. H. (2014). Gas Leakage Detection Using Thermal Imaging Technique. *2014 UKSim-AMSS 16th International Conference on Computer Modelling and Simulation*, 302–306. https://doi.org/10.1109/UKSim.2014.95

Jimenez, V. J., Bouhmala, N., & Gausdal, A. H. (2020). Developing a predictive maintenance model for vessel machinery. *Journal of Ocean Engineering and Science*, *5*(4), 358–386. https://doi.org/10.1016/j.joes.2020.03.003

Kistler. (2019). *Instruction Manual*. Kistler Group.

Krogerus, T., Björkqvist, J., & Niemi, S. (2018). *Research plan: EDGE - Edge Analytics for Smart Diagnostics in Digital Machinery Concept*.

Nawrat, A., Skorek, J., Jedrasiak, K., Daniec, K., Kostowski, W., Koteras, R., Czornik, A., Mendecka, B., Jarczyk, D., & Kasprzak, D. (2012). Application of IR thermography for evaluating the integrity of a natural gas delivery station. *Proceedings of the 13th International Carpathian Control Conference (ICCC)*, 515–520. https://doi.org/10.1109/CarpathianCC.2012.6228698

Noviantika, G. (2023, July 14). What Is CentOS – A Beginner’s Guide. *Hostinger Tutorials*. https://www.hostinger.com/tutorials/what-is-centos

Protacon. (2019). *Automaatiojärjstelmä järjestelmäkaavio*. [Restricted availability].

Protacon. (2020). Internal document. *All Modbus*. [Not published].

Raspberry Pi Ltd. (2019). *Rapberry Pi 4 Model B*. 2019 Raspberry Pi (Trading) Ltd.

Teledyne FLIR. (n.d.). *FLIR AX8*. FLIR. Retrieved September 19, 2023, from https://www.flir.eu/products/ax8-automation?vertical=rd+science&segment=solutions

Teledyne FLIR. (2019, June 24). *What is MSX®?* FLIR. https://www.flir.eu/discover/professional-tools/what-is-msx/

Teltonika Networks. (2022). *RUT950*. https://teltonika-networks.com/cdn/products/2023/01/63b7fbe20d9ae7-47483573/rut950-datasheet-v11.pdf

Wärtsilä. (2016). Internal document. *VEBIC, W4L20CR Diesel System Layout*. [Not published]

Wärtsilä. (2018a). *Wärtsilä 20 product guide*. Wärtsilä Finland Oy.

Wärtsilä. (2018b). *Wärtsilä 20 Engine Operation and Maintenance Manual*. Wärtsilä Finland Oy.

Appendices

Appendix 1. FLIR AX8 Datasheets

Table 14. FLIR AX8 communication and data storage details (modified from Teledyne FLIR, n.d.).

Attribute	Details
Ethernet	Control, result and image
Ethernet connector type	M12 8-pin X-coded
Ethernet power	PoE IEEE 802.3af class 0
Ethernet standard	IEEE 802.3
Ethernet type	100 Mbps
Ethernet video streaming	Yes
File formats	JPEG+FFF
Image storage mode	IR, visual, MSX®
Storage	Built-in

Table 15. FLIR AX8 imaging and optical details (modified from Teledyne FLIR, n.d.).

Attribute	Details
Automatic image adjustment	Yes, continuous
Built-in digital camera	640 × 480
Colour palettes	Black & white, black & white inversed, iron, rain
Detector type	FPA, uncooled microbolometer
Digital camera field of view	Adapts to the IR lens
Field of view	48 ° × 37 °
Focus	Fixed
Image modes	IR, visual MSX®
Image streaming formats	Motion JPEG, MPEG, H.264
Image streaming resolution	640 × 480
IR resolution	80 × 60
Sensitivity	10 Lux without illuminator
Spectral range	7,5 – 13 µm
Thermal Sensitivity/NETD	< 0,10 °C at 30 °C / 100 mK

Table 16. FLIR AX8 measurement capabilities (modified from Teledyne FLIR, n.d.).

Attribute	Details
Accuracy	±2 °C or ±2 % of reading (10 to 100 °C at 10 to 35 °C ambient)
Alarm functions	Automatic alarms on any selected measurement function. A maximum of 5 alarms can be set
Alarm output	DO, store image, file sending (ftp), email (SMTP), notification
Area	6 boxes with minimum, maximum and average
Atmospheric transmission correction	Automatic, based on inputs from distance, atmospheric temperature and relative humidity
Emissivity correction	Variable from 0.01 to 1.0
External optics & window correction	Automatic, based on input of optics/window transmission and temperature
Measurement corrections	Global object parameter
Object temperature range	– 10 to 150 °C
Optics transmission correction	Automatic, based on signals from internal sensors
Reflected apparent temperature correction	Automatic, based on input of reflected temperature
Set-up commands	Date/time, temperature °C/°F
Spot meter	Maximum 6

Table 17. FLIR AX8 Specifications environmental and certifications (modified from Teledyne FLIR, n.d.).

Attribute	Details
Bump	25 g (IEC 60068-2-29)
Electromagnetic compatibility	EN 61000-6-2:2001 (immunity) EN 61000-6-3:2001 (emission) FCC 47 CFR Part 15 Class B (emission)
Encapsulation	IP67 (IEC 60529)
Humidity	IEC 60068-2-30/24 h 95 % relative humidity 25 – 40 °C / 2 cycles
Operating temperature	0 – 50 °C
Storage temperature	– 40 – 70 °C IEC 68-2-1 and IEC 68-2-2
Vibration	2 g (IEC 60068-2-6)

Table 18. FLIR AX8 power connection details (modified from Teledyne FLIR, n.d.).

Attribute	**Details**
External power connector type	M12 8-pin A-coded (shared with digital I/O)
External power operation	12/24 VDC, 2 W continuously, 3,1 W absolute maximum
Voltage allowed range	10,8 – 30 VDC

Appendix 2. Legacy system signal list

Table 19. List of signals for Adlink data collection purposes (modified from Protacon, 2020).

Signal Source	Signal Description	Unit
Speedgoat	Variable inlet valve closing control position	
Speedgoat	Speed load mode	
Speedgoat	Speed load mode idle	
Speedgoat	Droop mode active	
Speedgoat	KW-mode active	
Speedgoat	Diesel balancing none mode	
Speedgoat	Diesel balancing temperature mode	
Speedgoat	Diesel balancing MEP mode	
Speedgoat	LO level low wet sump	
Speedgoat	External emergency	
Speedgoat	FO leakage	
Speedgoat	Generator breaker	
Speedgoat	External stop command	
Speedgoat	External stop/shut down	
Speedgoat	Engine stop	
PLC	Actual power	kW
PLC	Voltage	V
PLC	Frequency	Hz
PLC	Barometric pressure	mbar
PLC	Relative humidity	%
PLC	Ambient temperature	C
PLC	Generator Winding L1 temperature	C
PLC	Generator Winding L2 temperature	C
PLC	Generator Winding L3 temperature	C
PLC	Generator DE bear temperature	C
PLC	Generator nDE bear tmp	C
Speedgoat	Diesel pressure	bar
Speedgoat	HT pressure	bar
Speedgoat	LT water pressure	bar
Speedgoat	LO pressure	bar
Speedgoat	FO pressure	bar
Speedgoat	CA pressure	bar
Speedgoat	LO pressure 1	bar
Speedgoat	LO pressure 2	bar
Speedgoat	Crank case pressure	mbar
Speedgoat	Engine load	kW
Speedgoat	Pressure CA before CAC	bar
Speedgoat	LT cooling	%
Speedgoat	Analogue speed reference	rpm
Speedgoat	Engine load kW	kW
Speedgoat	Measured engine speed	rpm
Speedgoat	External load reference	kW
Speedgoat	Load reference kW	kW
Speedgoat	Fuel demand	
Speedgoat	Diesel demand	
Speedgoat	FCV position	
Speedgoat	AWG position	
Speedgoat	Miller timing on/off	deg
Speedgoat	Heat release at CA5, cyl1	deg
Speedgoat	Heat release at CA5, cyl2	deg
Speedgoat	Heat release at CA5, cyl3	deg
Speedgoat	Heat release at CA5, cyl4	deg

Signal Source	Signal Description	Unit
Speedgoat	Heat release at CA10, cyl1	deg
Speedgoat	Heat release at CA10, cyl2	deg
Speedgoat	Heat release at CA10, cyl3	deg
Speedgoat	Heat release at CA10, cyl4	deg
Speedgoat	Heat release at CA17,5, cyl1	deg
Speedgoat	Heat release at CA17,5, cyl2	deg
Speedgoat	Heat release at CA17,5, cyl3	deg
Speedgoat	Heat release at CA17,5, cyl4	deg
Speedgoat	Heat release at CA25, cyl1	deg
Speedgoat	Heat release at CA25, cyl2	deg
Speedgoat	Heat release at CA25, cyl3	deg
Speedgoat	Heat release at CA25, cyl4	deg
Speedgoat	Heat release at CA50, cyl1	deg
Speedgoat	Heat release at CA50, cyl2	deg
Speedgoat	Heat release at CA50, cyl3	deg
Speedgoat	Heat release at CA50, cyl4	deg
Speedgoat	Heat release at CA75, cyl1	deg
Speedgoat	Heat release at CA75, cyl2	deg
Speedgoat	Heat release at CA75, cyl3	deg
Speedgoat	Heat release at CA75, cyl4	deg
Speedgoat	Heat release at CA82,5, cyl1	deg
Speedgoat	Heat release at CA82,5, cyl2	deg
Speedgoat	Heat release at CA82,5, cyl3	deg
Speedgoat	Heat release at CA82,5, cyl4	deg
Speedgoat	Heat release at CA90, cyl1	deg
Speedgoat	Heat release at CA90, cyl2	deg
Speedgoat	Heat release at CA90, cyl3	deg
Speedgoat	Heat release at CA90, cyl4	deg
Speedgoat	Indicated mean effective pressure net cyl1	bar
Speedgoat	Indicated mean effective pressure net cyl2	bar
Speedgoat	Indicated mean effective pressure net cyl3	bar
Speedgoat	Indicated mean effective pressure net cyl4	bar
Speedgoat	Indicated mean effective pressure gross cyl1	bar
Speedgoat	Indicated mean effective pressure gross cyl2	bar
Speedgoat	Indicated mean effective pressure gross cyl3	bar
Speedgoat	Indicated mean effective pressure gross cyl4	bar
Speedgoat	Maximum pressure cyl1	bar
Speedgoat	Maximum pressure cyl2	bar
Speedgoat	Maximum pressure cyl3	bar
Speedgoat	Maximum pressure cyl4	bar
Speedgoat	Diesel injection 1 start timing cyl1	deg
Speedgoat	Diesel injection 1 start timing cyl2	deg
Speedgoat	Diesel injection 1 start timing cyl3	deg
Speedgoat	Diesel injection 1 start timing cyl4	deg
Speedgoat	Diesel injection 2 start timing cyl1	deg
Speedgoat	Diesel injection 2 start timing cyl2	deg
Speedgoat	Diesel injection 2 start timing cyl3	deg
Speedgoat	Diesel injection 2 start timing cyl4	deg
Speedgoat	Diesel injection 3 start timing cyl1	deg
Speedgoat	Diesel injection 3 start timing cyl2	deg
Speedgoat	Diesel injection 3 start timing cyl3	deg
Speedgoat	Diesel injection 3 start timing cyl4	deg
Speedgoat	Diesel injection 4 start timing cyl1	deg
Speedgoat	Diesel injection 4 start timing cyl2	deg
Speedgoat	Diesel injection 4 start timing cyl3	deg
Speedgoat	Diesel injection 4 start timing cyl4	deg
Speedgoat	Diesel injection 5 start timing cyl1	deg
Speedgoat	Diesel injection 5 start timing cyl2	deg

Signal Source	**Signal Description**	**Unit**
Speedgoat	Diesel injection 5 start timing cyl3	deg
Speedgoat	Diesel injection 5 start timing cyl4	deg
Speedgoat	Diesel injection 1 stop timing cyl1	deg
Speedgoat	Diesel injection 1 stop timing cyl2	deg
Speedgoat	Diesel injection 1 stop timing cyl3	deg
Speedgoat	Diesel injection 1 stop timing cyl4	deg
Speedgoat	Diesel injection 2 stop timing cyl1	deg
Speedgoat	Diesel injection 2 stop timing cyl2	deg
Speedgoat	Diesel injection 2 stop timing cyl3	deg
Speedgoat	Diesel injection 2 stop timing cyl4	deg
Speedgoat	Diesel injection 3 stop timing cyl1	deg
Speedgoat	Diesel injection 3 stop timing cyl2	deg
Speedgoat	Diesel injection 3 stop timing cyl3	deg
Speedgoat	Diesel injection 3 stop timing cyl4	deg
Speedgoat	Diesel injection 4 stop timing cyl1	deg
Speedgoat	Diesel injection 4 stop timing cyl2	deg
Speedgoat	Diesel injection 4 stop timing cyl3	deg
Speedgoat	Diesel injection 4 stop timing cyl4	deg
Speedgoat	Diesel injection 5 stop timing cyl1	deg
Speedgoat	Diesel injection 5 stop timing cyl2	deg
Speedgoat	Diesel injection 5 stop timing cyl3	deg
Speedgoat	Diesel injection 5 stop timing cyl4	deg
Speedgoat	Diesel duration 1 cyl1	µs
Speedgoat	Diesel duration 1 cyl2	µs
Speedgoat	Diesel duration 1 cyl3	µs
Speedgoat	Diesel duration 1 cyl4	µs
Speedgoat	Diesel duration 2 cyl1	µs
Speedgoat	Diesel duration 2 cyl2	µs
Speedgoat	Diesel duration 2 cyl3	µs
Speedgoat	Diesel duration 2 cyl4	µs
Speedgoat	Diesel duration 3 cyl1	µs
Speedgoat	Diesel duration 3 cyl2	µs
Speedgoat	Diesel duration 3 cyl3	µs
Speedgoat	Diesel duration 3 cyl4	µs
Speedgoat	Diesel duration 4 cyl1	µs
Speedgoat	Diesel duration 4 cyl2	µs
Speedgoat	Diesel duration 4 cyl3	µs
Speedgoat	Diesel duration 4 cyl4	µs
Speedgoat	Diesel duration 5 cyl1	µs
Speedgoat	Diesel duration 5 cyl2	µs
Speedgoat	Diesel duration 5 cyl3	µs
Speedgoat	Diesel duration 5 cyl4	µs
Speedgoat	Main fuel injection offsets diesel cyl 1	%
Speedgoat	Main fuel injection offsets diesel cyl 2	%
Speedgoat	Main fuel injection offsets diesel cyl 3	%
Speedgoat	Main fuel injection offsets diesel cyl 4	%
Speedgoat	Cylinder pressure max rise rate cyl 1	bar/deg
Speedgoat	Cylinder pressure max rise rate cyl 2	bar/deg
Speedgoat	Cylinder pressure max rise rate cyl 3	bar/deg
Speedgoat	Cylinder pressure max rise rate cyl 4	bar/deg
Speedgoat	Cylinder pressure max rise rate location cyl 1	deg
Speedgoat	Cylinder pressure max rise rate location cyl 2	deg
Speedgoat	Cylinder pressure max rise rate location cyl 3	deg
Speedgoat	Cylinder pressure max rise rate location cyl 4	deg

Appendix 3. Equipment figures

Figure 24. The water expansion tank from outside (left) and inside (middle). The water level can be read from the side (right).

Figure 25. The clean leak fuel tank.

Appendix 4. Engine operation schedules during the experiments of exhaust gas leakage

Table 20. No leakage 3.3.2020

Command	Timestamp	From engine start	Time spent at point
Start	12:25:26	00:00:00	00:17:30
Load 25 %	12:42:56	00:17:30	00:06:34
Load 50 %	12:49:30	00:24:04	00:07:41
Load 75 %	12:57:11	00:31:45	00:08:02
Load 100 %	13:05:13	00:39:47	00:15:41
Load 50 %	13:20:54	00:55:28	00:08:21
Load 0 %	13:29:15	01:03:49	00:08:25
Shutdown	13:37:40	01:12:14	

Table 21. No leakage 16.3.2020

Command	Timestamp	From engine start	Time spent at point
Start	09:47:03	00:00:00	00:17:47
Load 25 %	10:04:50	00:17:47	00:06:39
Load 50 %	10:11:29	00:24:26	00:07:41
Load 75 %	10:19:10	00:32:07	00:08:05
Load 100 %	10:27:15	00:40:12	00:15:51
Load 50 %	10:43:06	00:56:03	00:08:33
Load 0 %	10:51:39	01:04:36	00:08:23
Shutdown	11:00:02	01:12:49	

Table 22. Artificial leakage 4.3.2020

Command	Timestamp	From engine start	Time spent at point
Start	10:06:03	00:00:00	00:16:55
Load 25 %	10:22:58	00:16:55	00:06:09
Load 50 %	10:29:07	00:23:04	00:05:47
Load 75 %	10:34:54	00:28:51	00:05:51
Load 100 %	10:40:45	00:34:42	00:21:26
Load 50 %	11:02:11	00:56:08	00:10:30
Load 0 %	11:12:41	01:06:38	00:08:55
Shutdown	11:21:36	01:15:33	

Table 23. Artificial leakage 12.3.2020

Command	Timestamp	From engine start	Time spent at point
Start	12:19:32	00:00:00	00:17:09
Load 25 %	12:36:41	00:17:09	00:06:36
Load 50 %	12:43:17	00:23:45	00:05:50
Load 75 %	12:49:07	00:29:35	00:05:54
Load 100 %	12:55:01	00:35:29	00:21:32
Load 50 %	13:16:33	00:57:01	00:10:36
Load 0 %	13:27:09	01:07:37	00:09:17
Shutdown	13:36:26	01:16:54	

Appendix 5. Thermal images

Figure 26. Temperatures at the load command to 25 %. No leakage on the left, artificial leakage on the right. Experiments on 27.11.2019 & 28.11.2020.

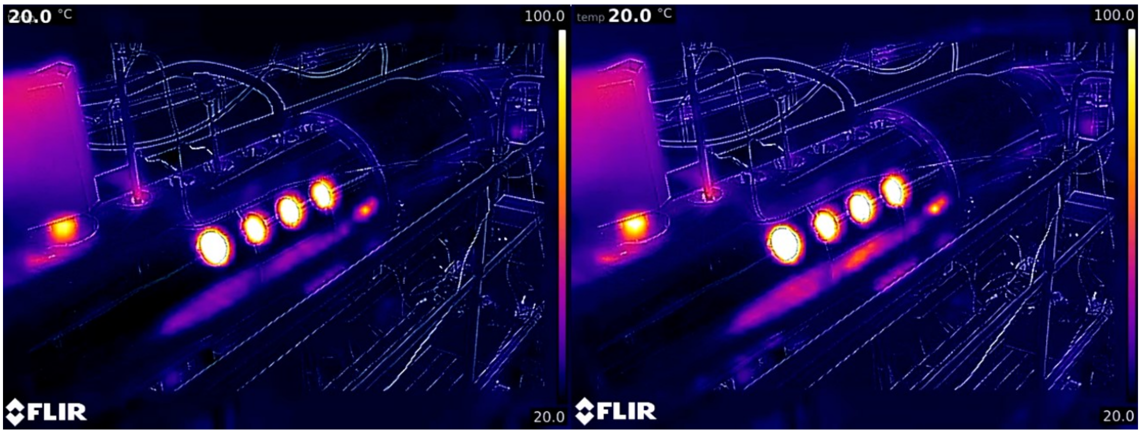

Figure 27. Temperatures at the load command to 50 %. No leakage on the left, artificial leakage on the right. Experiments on 27.11.2019 & 28.11.2020.

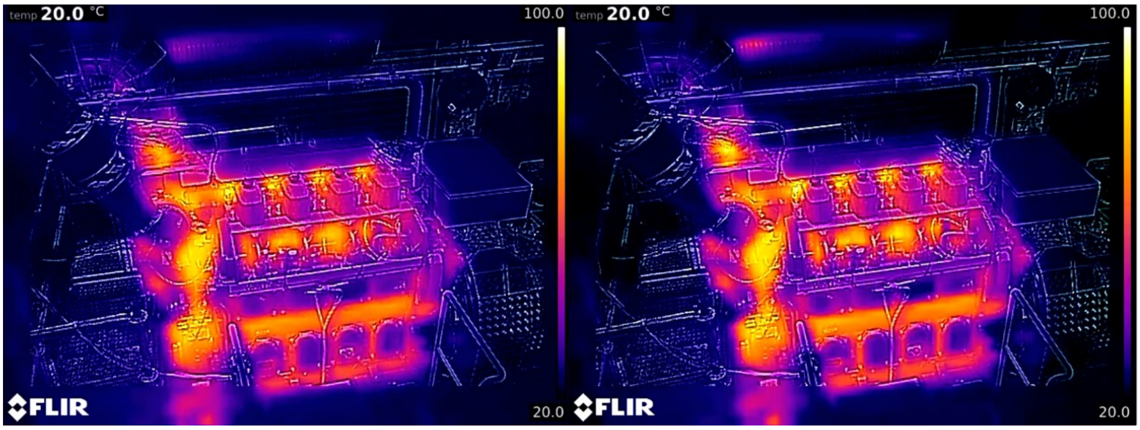

Figure 28. Temperatures at the load command to 50 %. No leakage on the left, artificial leakage on the right. Experiment on 3.3.2020 & 4.3.2020.

Figure 29. Temperatures at the load command to 75 %. No leakage on the left, artificial leakage on the right. Experiments on 3.3.2020 & 4.3.2020.

Figure 30. Temperatures at the load command to 100 %. No leakage on the left, artificial leakage on the right. Experiments on 3.3.2020 & 4.3.2020.

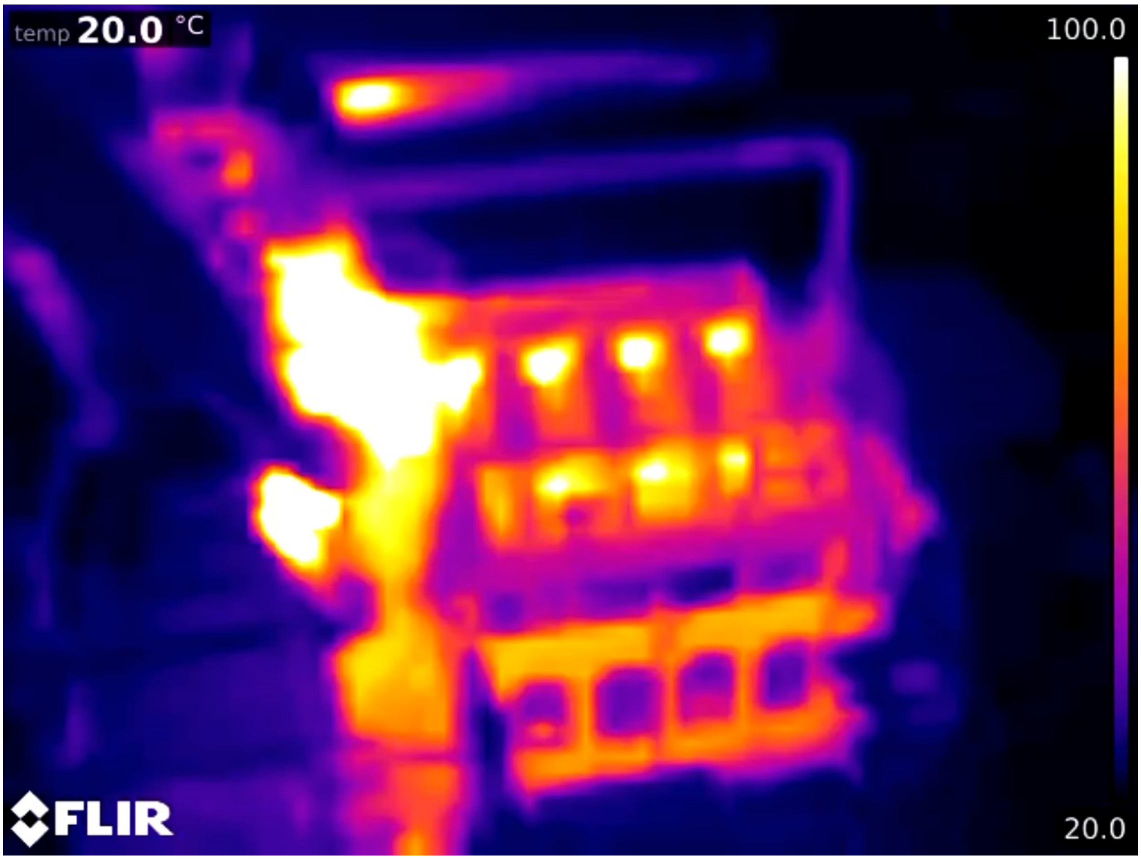

Figure 31. Reference on how the engine thermal profile looks like with the pure IR mode. Taken during full load with induced artificial leakage on 4.3.2020 at 10:59:05.

Figure 32. Reference on how the engine thermal profile looks like with the pure IR mode. Taken when ramping the engine down at 50 % load without the induced artificial leakage on 3.3.2020 at 13:22:17.

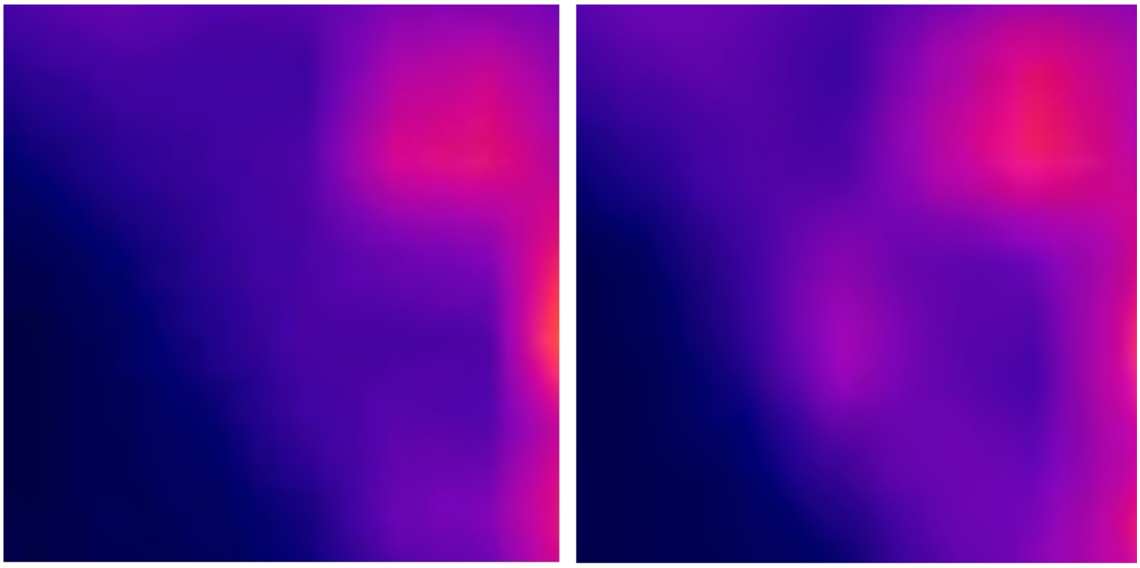

Figure 33. Zoomed in comparison between IR materials on 3.3.2020 (left) and 4.3.2020 (right).